POLITECNICO
MILANO 1863

SCUOLA DI INGEGNERIA INDUSTRIALE
E DELL'INFORMAZIONE

Thermal Model and Analysis of the LUMIO-Cam

Master degree thesis - Tesi di Laurea Magistrale in Space Engineering - Ingegneria Spaziale

Author: **Giovanni Carbone**

Student ID: 970633
Supervisor: Prof. Francesco Topputo
Co-supervisor: Dr. Vittorio Franzese
Academic Year: 2021-22

Abstract

LUMIO is a 12 U cubesat designed to orbit at L2 point in the Earth-Moon system to observe meteoroid impacts on the Lunar farside. The main payload is the LUMIO-Cam: an optical instrument specifically designed for this mission by Leonardo S.p.A. The LUMIO-Cam will be able to perform simultaneous observation in two different wavebands (VIS and NIR) to autonomously identify meteoroid impacts. To ensure a good SNR for these measurements, a strict temperature control of the detectors must be performed to maintain a constant value of -20°C.
In this thesis work a complete thermal model of the instrument is built, based on the final output of phase-A and analyses to proceed with the phase-B design are carried out. The GMM and TMM of the instrument have been created on a dedicated software for thermal analysis and simulations were performed to analyse the behaviour of the instrument.
The first study is focused on the capability of the detectors to withstand direct Sun exposure without being damaged. The obtained results confirmed that the instrument does not need a mechanical shutter for protection of its detectors. The second set of analyses was performed to ensure that the entire instrument is compliant with the non-operational temperature limit requirement. This set of analyses gave positive outcome as well. Lastly a preliminary analysis of operational conditions is performed with the sole objective of assessing the ability of the system of stabilizing the detectors temperature at -20°C. In this case the results obtained with the phase-A were unsatisfactory and minor design changes had to be made to reach the temperature goal.
The next steps in the advancement of LUMIO-Cam design involve updating the model and performing more detailed analyses. The new thermal model of the instrument is needed to keep track of the changes deriving from SRR. The analyses will be repeated to ensure that the new deign is compliant to every requirement.

Keywords: LUMIO-Cam, requirement, thermal model, survivability

Abstract in lingua italiana

LUMIO è un cubesat da 12 unità progettato per orbitare nel punto lagrangiano L2 del sistema Terra-Luna con l'obiettivo di osservare l'impatto dei meteoroidi sul lato nascosto della superficie lunare. Lo strumento principale è la LUMIO-Cam, uno strumento ottico progettato appositamente per questa missione da Leonardo S.p.A. Questo strumento è in grado di identificare autnomamente l'impatto dei meteoroidi grazie ad un'acquisizione simultanea su due canali (VIS e NIR) delle immagini. Per garantire una buona qualità delle misurazioni è necessario un controllo termico attivo sui detector per mantenerli a una temperatura costante di -20°C.
L'obiettivo di questa tesi è quello di creare un modello termico completo dello strumento, basato sul design finale della fase A, e di eseguire delle analisi che permetteranno di procedere con il design di fase B dello stesso. Il GMM e TMM della LUMIO-Cam sono stati creati e analizzati su un software specifico per analisi termiche.
Il primo set di analisi serve a stabilire la capacità dei detector di resistere a un'esposizione diretta al Sole senza danneggiarsi. I risultati hanno confermato questa capicità escludendo quindi la necessità di un otturatore meccanico per proteggere i sensori. Il secondo set di analisi è stato eseguito per verificare che il design consentisse allo struemnto di rispettare i requisiti di sopravvivenza in condizioni non operative. Anche in questo caso i risultati hanno confermato la validità del design che risulta quindi in linea con i requisiti di sistema. L'ultimo studio è incentrato esclusivamente a stabilire la capacità dello strumento di mantenere i sensori alla temperatura desisderata di -20°C. Il design di fase A è risultato essere inadatto e delle migliorie sono state necessarie per garantire il raggiungimento dell'obiettivo.
I prossimi passaggi nello sviluppo della LUMIO-Cam prevedono un aggiornamento del modello termico e l'esecuzione di analisi più dettaglaite. Questo nuovo modello servirà a incorporare le novità nel design della LUMIO-Cam derivanti dalla SRR. Su questo nuovo modello andranno poi ripetute le analisi per assicurarsi che tutti i requisiti vengano rispettati.

Parole chiave: LUMIO-Cam, requisito, modello termico, sopravvivenza

Contents

1 | Introduction

One of the biggest natural threats for mankind is the possibility that a celestial body may one day hit our planet leading to catastrophic consequences and ultimately to the extinction of our species. Although this sci-fi scenario may seem unlikely, thousands of objects are constantly travelling in space towards us at high velocity and it is not rare they have not been identified yet. The main example one could make is the Čeljabinsk meteor that entered in the atmosphere above Russia's skies on 15 February 2013 undetected. The object was estimated to be around 10000 tonnes and exploded at an altitude of 30-50 km above ground releasing an energy equivalent to 500 ktons. This event fortunately didn't lead to any casualties but a lot of people were injured and the damages were considerable. This example should make us realize how powerless we are to the unknown and the importance of meteoroid catalogues that describe exactly what is around us in space. This knowledge would allow the application of countermeasures if necessary, an example of such possible countermeasure is the DART mission that successfully deflected Dimorphos' orbit.

Another aspect for which the knowledge of meteoroid flux is crucial is the newly renovated interest of mankind for lunar exploration. The possibility of exploiting other planets to mine their resources is becoming every day more interesting and this has led to a new campaign of lunar mission with the ultimate objective of building a stable base on the Moon. The seemingly calm lunar environment appears ideal to host a human outpost but the reality is quite different. Being atmosphere-free, the Moon lacks the basic protection from even the smallest meteoroid that could cause irreversible damages to any human structure present on the surface. This factor was not considered problematic for short term missions as those of the Apollo program but it must be taken into account if much bigger efforts are to be made in the building of a stable base. For this reason it is also important to learn more about the meteoroid flux on our natural satellite.

1.1. Current meteoroids observation

The current database of NEOs (Near Earth Objects) has been built in the last 50 years thanks to continuous observations and studies by national agencies and by amateurs. The database has in fact always been available to the general public together with and all the information about meteoroid detection so that anyone willing to cooperate can help in enriching the knowledge.
There are two main strategies for detecting a meteoroid that can be identified as *direct* and *indirect*. The first is based on meteoroid observation while the second studies their impacts (meteors).
The so called direct method consists in exploiting terrestrial and space telescopes to acquire subsequent images of a portion of the sky to be analyzed in search of meteoroids. The software isolates fixed stars and ignores them thus keeping only transient objects; if one is found, first a match in the meteoroid database is searched, in case there is no match, the object is added to a list of bodies to be verified and additional images of it are taken to have larger amount of data to analyse to increase the precision of the following calculations. If the preliminary analyses indicate that there is the risk of collision with Earth, the object is given maximum priority. The main example of this first method is the Planetary Defense program ([12]) established in January 2016 and coordinated by NASA which aims at identifying and cataloguing potentially hazardous NEOs. This program is based on the integration and cooperation of different missions (like the NEOWISE project), observatories (like the Infrared Telescope Facility) and NEO survey programes (like those of the university of Arizona and Hawaii) to acquire information about known NEOs and possibly detect new ones. When a new NEO is discovered, the informations are given to the Center for Near-Earth Object Studies to be analysed and later catalogued by the Minor Planet Center. In the end a risk analysis and mitigation study is performed, the most recent success in this field is the already mentioned DART mission.
The second method is called indirect because it studies meteors. This technique consists in observing impacts and studying their characteristics; this allows to retrieve the main informations and properties of the original meteoroid. It is clear that this method does not allow to foresee any collision between the meteoroid and our planet but it is extremely valuable to characterize from a statistical point of view the population of space objects orbiting near Earth and validate existing models. The main observation target for this type of analysis is the Moon as the absence of an atmosphere allows meteors of any dimension to hit the surface. The best example for this kind of analysis is NELIOTA, better explained in [1.1.1].
An important aspect that additionally differentiates the two methods is the fact that with

the indirect method it is possible to detect sub-meter objects (something that is nearly impossible to do with a direct observation method) with the inferior limit being related to the sensitivity of the cameras used to observe the flashes of the impacts. Both direct and indirect method suffer from various limitations when the observations are performed from Earth's surface that are caused by the atmosphere. While for the active observation of meteoroids, different satellites have been used or have by accident contributed to the discovery of new bodies; there are few satellites that can be helpful in the study of lunar meteor impacts. In this context, the newly designed mission LUMIO (Lunar Meteoroid Impact Observer) is a breakthrough for improving the knowledge of meteoroid flux in our environment.

1.1.1. NELIOTA

NELIOTA is the newest and most powerful program that performs an indirect type of analysis. The program began operation on 8 March 2017, under European Space Agency funding and is operated by the National Observatory of Athens. The 1.2 m telescope is equipped with a dichroic that splits the incoming light in two channels with a cutoff wavelength of 730 nm. The light is then recorded by advanced digital cameras allowing to capture flashes due to meteor impact with high accuracy with a single telescope, something that was never done before. This is possible thanks to the automatic post-processing operated by the dedicated software that is able to identify and retain as impact flashes only those events that occur simultaneously in both channels. Since the beginning of operations, 172 impacts have been recorded and confirmed in just under 250 hours of observation, and the statistics are made public on the website [13]. In Fig.(1.1) are reported the graphics of observed hours and recorded events with respect to the observation period. The biggest limitations to NELIOTA's observations are connected to the fact that they are performed from ground:

- **Atmosphere:** the atmospheric presence has negative effects on the measurements as it attenuates the signal received on ground and it also requires frequent re-calibration of the instrument.
- **Weather:** if the skies above the telescope are cloudy, no observation can be performed.
- **Day/night cycle:** Earth bound observations for impact flash detection can only be performed at night, reducing the available observation time.
- **Latitude and longitude:** when observing the Moon from Earth, it is impossible to study polar regions and, in some periods, the central meridian.

- **Lunar surface visibility:** the synchrony between Moon's orbital period and its rotation around the axis is such that from Earth's surface only one side of the satellite is visible at all times (nearside).

Another limitation to flash detection that is not connected to being performed from Earth is the Moon illumination condition: the flashes are visible only when $< 50\%$ of the lunar surface is lit by the Sun.

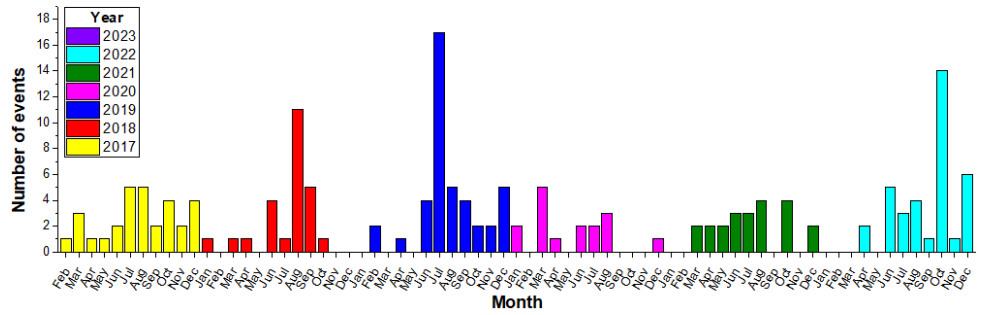

(a) *Distribution of events in time*

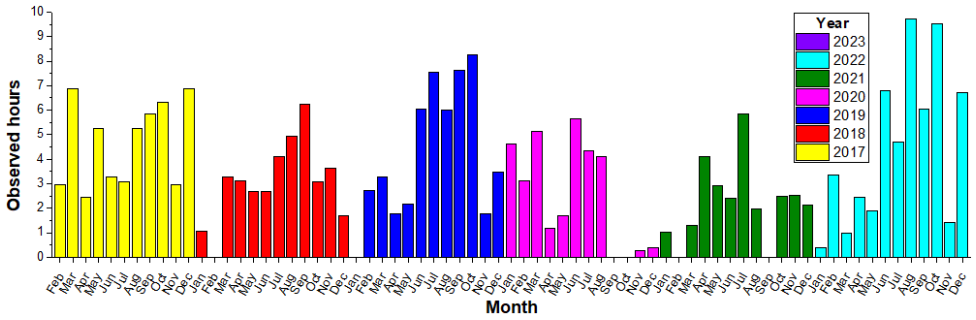

(b) *Distribution of observed hours in time*

Figure 1.1: NELIOTA statistics

1.2. Lunar meteoroid flux

The measurements done to this day have led to the estimation of the interval of velocities at which an impact may happen between the Earth or Moon and a meteoroid. For what concerns the Earth, the minimum impact velocity is equal to the escape velocity of the planet, $v_{escape} = 11.2\ km/s$. The maximum impact velocity would happen under the condition in which the Earth encounters a body at the perihelion of its retrograde, highly elliptic orbit, the sum of the two velocities would be $v_{max} = 72.8\ km/s$. Considering that the Moon has a relative velocity with respect to Earth of 1 km/s, the impact velocity interval for the Moon would be $10.2 - 73.8\ km/s$. These values are valid for meteor showers (in general, being originated by comets, meteoroid showers have higher velocities than meteoroids from sporadic sources); for what concerns meteoroids from sporadic

sources the literature has different values: some use 17 *km/s* and other 24 *km/s* when targeting the Moon. The European Cooperation for Space Standardization (ECSS) uses a distribution between $0.5 - 71.5$ *km/s* when targeting Earth in its models.
A factor that could alter these velocities is related to the gravitational attraction of the Earth-Moon system which has a double effect: 1) *gravitational acceleration* causes the impactor to gain velocity before hitting the surface, 2) *gravitational focusing* actually increases the number of impacts. The actual magnitude of these two effects depends on the impactor's velocity and other characteristics but, in general, both effects are significant for Earth and negligible for the Moon.
The lunar meteoroid impact flux models available to date are different and not always in agreement: some estimate a flux of 1290 impacts per year while other have values of 4000 impacts per year for a > 1 *kg* impactor [3]. One critical aspect on which all models seem to agree is the presence of asymmetries in the impact distribution on Moon's surface:

- The lunar nearside has 0.1% more impacts than the farside due to Earth's gravity field.
- The equatorial flux is $10 - 20\%$ larger than polar regions due to the higher concentration of meteoroids in low inclination orbits.
- The Moon's leading side has an estimated $37 - 80\%$ higher flux than the trailing side because of Moon's synchronous rotation. This asymmetry could be explained by a higher impact velocity on the leading side resulting in ease to detect impacts but it is not certain. Thus, full-disk observations of the Moon are necessary to understand the apex/antapex asymmetry.

During an impact the kinetic energy of the meteoroid is split in four contributions: 1) the generation of a seismic wave, 2) the excavation of a crater, 3) the ejection of particles, 4) the emission of radiation. All these phenomena can, in theory, be exploited to detect an impact.

1. **Seismic waves:** to be detected it is necessary to place in-situ some seismic station and the coverage of each of them is limited. Moreover, this technique does not allow to identify meteoroid impacts by itself nor it is possible to retrieve independent impactor informations.
2. **Crater excavation:** exploits the generation of new craters to detect an impact. The process is time consuming given the high amount of data to be processed but it allows to perform remote sensing and to have 100 % coverage of the lunar surface. The major downside is the impossibility to determine the time of impact and other

important characteristics of the meteoroid.

3. **Particle ejection:** requires in-situ placement of particle detectors and has a very low surface covering for each of them. It is possible to independently identify meteoroid impacts but the time instant and location of the impact cannot be determined.

4. **Radiation:** is emitted in both the visible and infrared spectrum; the equivalent impact temperature is estimated to be $1700 - 2000\ K$. Allows cover up to 50 % of the Moon's surface and with this method it is possible to determine the position and time instant of the impact together with the actual flash temperature and the impactor's kinetic energy (mass and/or velocity).

By performing a trade-off between these four detection methods, it is easy determined that the best solution is to observe flashes. This logic has been adopted in the development of LUMIO and its payload, the LUMIO-Cam.

1.3. LUMIO

This section summarizes all the main aspects of LUMIO (Lunar Meteoroid Impact Observer), the mission which payload is at the center of the analyses of this thesis.

1.3.1. Context and importance of LUMIO

As previously mentioned in the introduction of this chapter, one of the objectives of the present day space research is to better characterize the asteroid flux for reasons of planetary protection and to improve our knowledge of the lunar environment for future exploration missions on its soil. A big contribution to this goal will derive from LUMIO which can be defined as follows:
"*LUMIO is a CubeSat mission to a halo orbit at Earth–Moon L2 that shall observe, quantify, and characterise meteoroid impacts on the Lunar farside by detecting their flashes, complementing Earth-based observations on the Lunar nearside, to provide global information on the Lunar Meteoroid Environment and contribute to Lunar Situational Awareness.*"[3].
The mission, which entered phase-B of the design in September 2022, is one of the two winners of ESA's LUCE (Lunar CubeSat for Exploration) SysNova competition of 2018 and is being developed by a consortium headed by the DART team of Politecnico di Milano to address the following three main points [3]:

- **Science question:** What are the spatial and temporal characteristics of meteoroids impacting the lunar surface?

- **Science goal:** Advance the understanding of how meteoroids evolve in the cislunar space by observing the flashes produced by their impacts with the lunar surface.
- **Science objective:** Characterise the flux of meteoroids impacting the lunar surface.

The baseline is to use a 12 U cubesat (that will be deployed as secondary payload) to host the LUMIO-Cam, the optical instrument that will be used to detect the impacts on the lunar surface. LUMIO is especially important because it has been designed to observe the lunar farside (a better explanation of how this is performed will be in [1.3.3]). This design choice makes LUMIO's measurements even more valuable as they will be complementary to those of NELIOTA. Moreover, LUMIO will also be able to record fainter signals associated to much smaller meteorite impacts because their signals will not be attenuated by the presence of an atmosphere.
An aspect that further increases LUMIO's value is its technology demonstration objective: during the mission an experiment for cubesat autonomous navigation will be carried out.

1.3.2. Mission objectives

The main mission objectives are reported hereafter, and have been taken by the official LUMIO System Design Report [6]:

Objective ID	**Objective**	Stakeholder
MO.01	To conduct observations of the lunar surface in order to detect meteoroid impacts and characterise their flux, magnitudes, luminous energies, and sizes.	ESA
MO.02	To complement observations achievable via ground-based assets in space, time, and quality in order to provide a better understanding of the meteoroid environment.	ESA

Table 1.1: Mission objectives

Objective ID	Objective	Stakeholder
TLO.01	To perform remote sensing of the lunar surface and measurement of astronomical observations not achievable by past, current, or planned lunar missions.	ESA
TLO.02	To demonstrate deployment and autonomous operation of CubeSats in lunar environment, including localization and navigation aspects.	ESA
TLO.03	To demonstrate miniaturization of optical instrumentation and associate technology in lunar environment.	ESA
TLO.04	To perform inter-satellite link to a larger Lunar Orbiter for relay of data and for TTC.	ESA

Table 1.2: Top-level objectives

1.3.3. Mission profile

The overall lifetime of LUMIO can be split in five main phases, schematically represented in Fig.(1.2):

1. **Earth-Moon transfer:** the satellite is connected to the carrier and the systems are switched off.
2. **Parking phase:** the satellite is released from the carrier, de-tumbling is performed before deploying the solar arrays and finally all the subsystems are commissioned.
3. **Transfer phase:** is characterized by four maneuvers; a Stable Manifold Injection Maneuver (SMIM), two trajectory correction maneuvers, and one Halo Injection Maneuver (HIM).
4. **Operative orbit:** will last approximately one year and is divided in two repetitive cycles, a science cycle and a navigation and engineering cycle.
5. **End of life:** the systems are decommissioned and the satellite is removed from the halo orbit to ensure that it will not harm any space asset in the lunar environment.

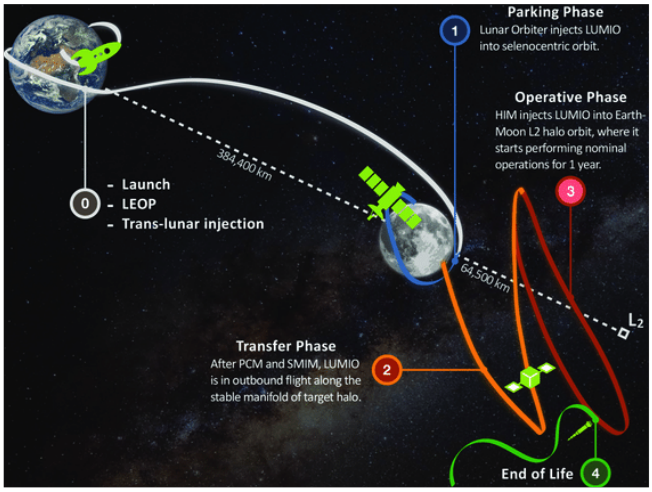

Figure 1.2: LUMIO baseline phases

The operative orbit selected for LUMIO's nominal operations is a halo orbit at L2 libration point in the Earth-Moon system. This means that the spacecraft will be always facing the lunar farside. In particular the orbit has a Jacobi constant $C_j = 3.09$; this selection is the result of a trade-off performed on 14 different quasi-halo orbits computed in a high-fidelity Roto-Pulsating Restricted n-Body Problem.
The selected orbit, when studied in a circular restricted three body problem, results in a locked 2:1 resonance which means 2 satellite orbits per synodic period ($T_{syn} = 29.4873$ days). This resonance allows the satellite to perform cyclical operations being divided in a *Science Orbit* and in a *Navigation and Engineering Orbit*. The two cycles are schematically represented in Fig.(1.4). Along the Science orbit the science cycle is performed, in this time (between first and last quarter, when lunar surface illumination is $< 50\%$) the satellite is oriented to maintain the LUMIO-Cam pointed towards the center of the Moon to detect impact flashes. The acquired images are processed to be compressed and are sent to earth thanks to a DTE (Direct To Earth) downlink. During the Navigation and Engineering Orbit (from last quarter to first quarter), the Nav&Eng cycle takes place. In this case the satellite changes its orientation to face the solar panels towards the sun for power generation, performs reaction wheel desaturation and station keeping maneuvers and the DTE link is exploited for orbit determination. This time is also exploited to perform the autonomous navigation experiment since high surface illumination condition is optimal. The different pointings for the two cycles is graphically represented in Fig (1.3).
The two cycles last approximately 14.8 days (Scientific) and 13.3 (Nav&Eng) and in total both are performed 13 times in a one-year operational timespan. In the real case un-

fortunately the 2:1 resonance is not exact, rather the satellite's orbital period oscillates with variable amplitudes around a nominal value. This uncertainty in the actual orbit duration makes it difficult to precisely estimate the cycles duration and planning. The ideal solution would be switching from one cycle to the other based on the real time conditions experienced by the satellite instead of using a pre-fixed schedule but this option is too complex. The best trade-off is to plan the change of cycle in order to maximize the amount of data collected allowing the cycles to have a non-constant duration along the operational year. A more in depth analysis of this problem can be found in [4].

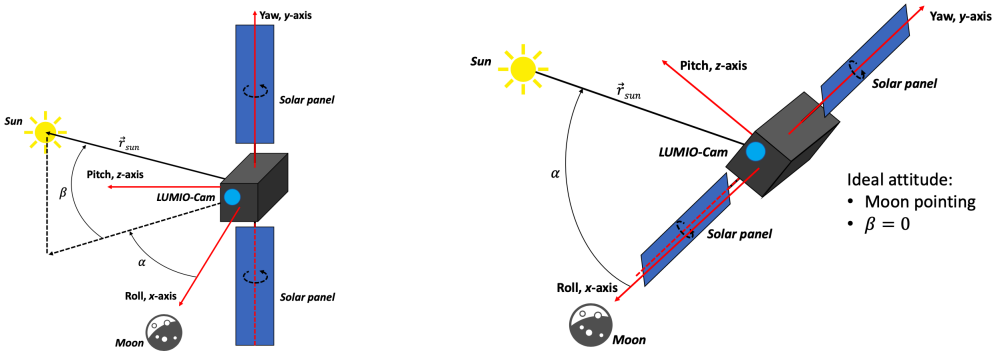

Figure 1.3: LUMIO poinint strategies for Science cycle (left) and Nav&Eng cycle (right).

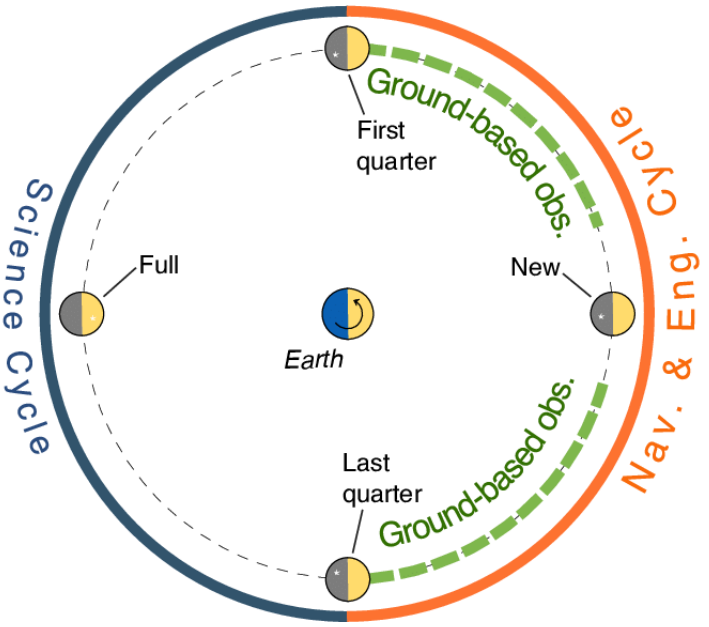

Figure 1.4: LUMIO conceptual cycles

1.3.4. Environment analysis

When designing a satellite it is fundamental to verify its ability of withstanding the operational environment conditions and that the performances are satisfying in every circumstance.
The launcher environment is the first to be encountered by the satellite. Since it is still unknown what vehicle will be used to put LUMIO in orbit, to allow the progression of the design, the considered envelope is such that all the most common launchers are a viable alternative.
The second environment to be analyzed is the open space for which the most critical aspect are radiations. The charged particles can damage electronic devices, decrease the efficiency of solar arrays and alter the optical properties of materials. LUMIO will encounter three main radiation environments during the five phases of its lifetime:

- **Trapped particles:** since the satellite will still be turned off in the first phase of the mission (piggiback) and since trapped particles are present only in the vicinity of Earth, their effects are neglected
- **Solar particles:** solar particle fluxes can be divided in two categories, Solar Flares and Coronal Mass Ejection (CME). The main differences between the two are spatial scale and speed: solar flares are localised and very fast while CMEs are more diffused and slower. Due to their low propagation speed, CME effects can be detected in advance and counteracted for example by turning off sensitive components. The model used for LUMIO is CREME-96 (available in SPENVIS) but other models are available.
- **Galactic cosmic rays**: background radiation always present coming from outside the solar system and are responsible for Single Event Effects (SEE). The shielding necessary to protect sensitive components from SEE is not achievable for space assets (too high) so it is important that devices can safely withstand this type of radiation without compromising mission performances.

The Total Ionizing Dose (TID), which is fundamental to estimate the amount of shielding necessary, has been computed in SPENVIS using a mission duration of 18 months to take into account the uncertainty in the launch date and the possibility that the satellite remains in the parking orbit for up to 6 months.
Of greatest interest for this thesis is the thermal environment to which LUMIO will be subject. The phases have been analysed grouped for their thermal environment similarities and the fluxes hitting the spacecraft have been estimated. To perform these preliminary analyses some assumptions were necessary to simplify calculations and to get

rid of uncertainties stopping the development:

- The Sun-satellite distance is assumed constant as a first approximation.
- Being the start date of the mission unknown, the average solar flux has been used for calculations.
- According to Mission Analysis, the satellite will not experience eclipse during transfer and operational phases.
- Along the parking orbit the satellite will experience eclipse.

In Tab.(1.3) are reported the heat fluxes computed in this preliminary analysis, the calculations for the E-M transfer used an Earth average albedo value of 35% and a black body temperature of 287 K while for the parking phase the lunar values were used (average albedo of 12%, black body temperature 271 K).

Flux type $[W/m^2]$	E-M transfer	Parking (hot)	Parking (cold)
Solar	1367	1367	1367
Albedo	4.41	147	5.2
Planet IR	3.54	273	9.7

Table 1.3: Heat fluxes

The analysis of the operational orbit is worth a more detailed discussion; for the hot case the configuration is such that the sun is perpendicular to the solar panels, two of the 6U body panels are illuminated by the Sun with a 45 deg incidence angle and the spacecraft is operating in science mode (power consumption is computed accordingly). The assumptions made in this case are for a worst case scenario thus the solar flux is set to the maximum value ($1420\,W/m^2$). The cold case scenario is again a worst case: since no eclipses are present along the operational orbit, the cold case is equivalent to least amount of power dissipated during normal operations with one 6U blank anodized panel is oriented towards the Sun (minimum flux due to low absorptivity of the surface). In this case the solar flux is set to the minimum value ($1380\,W/m^2$), and the solar panels are still at 90 deg with respect to the Sun. In both cases only solar flux and internal power dissipation have been considered because the closest celestial object is the moon at a distance of $30000\,km$ (IR and albedo fluxes are negligible at this distance).
More detailed information on all these environmental analyses can be found in [5].

1.3.5. System design

The main design choices and system aspects will be presented hereafter.

Payload

The payload (PL) for this mission is the LUMIO-Cam, an optical instrument to detect impact flashes. The instrument has a sensitive bandwidth that ranges between $450 - 950$ nm and is made of three main assemblies: the optical head (barrel and baffle), the focal plane assembly (FPA) and the proximity electronics.
The optical barrel contains 5 lenses with a focal length of 127 mm (F#=2,5) and a field of view (FOV) of $\pm 3°$. A dichroic (positioned after the lenses) is used to split the incoming radiation into two different channels (visible -VIS- and near infra-red -NIR-) at a wavelength of 820 nm. This two channels configuration is basically identical to the one used for NELIOTA and allows the estimation of the flash temperature thanks to the signal magnitude ratio in the two channels. The glass selection for the lenses is driven by optical quality and transmission characteristics. The space environment, being non-protected from high energy radiations, is especially challenging for optical instruments due to their intrinsic lack of shielding. Under these conditions the transmittance of glasses decreases in time thus reducing the system's SNR. The glasses selected for LUMIO are: CaF_2 (L1, L2), Lak_9G_{15} (L3, L5), F_2G_{12} (L4) and fused silica (beam splitter) (lens scheme in Fig.(1.5). This selection is the result of a trade-off between transmittance and radiation resistance (LUMIO's lenses are expected to be subject to a total exposure of 10 kRad overall).

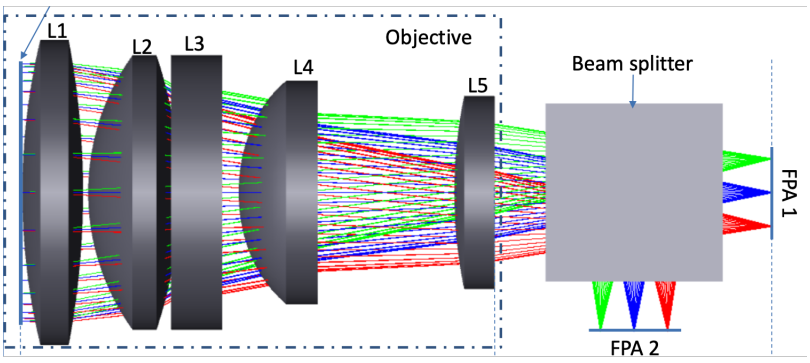

Figure 1.5: LUMIO optical scheme

A preliminary straylight rejection analysis considered a baffle length from 0 up to 200

mm (50 mm increments) in front of the optical barrel and a plane wave source at infinite distance forming an angle from 0° up to 45° (5° increments) with the camera line of sight to model the Sun (fraction of power reaching FPA normalised to the value at 0°). The results are reported in Fig.(1.6). From this preliminary analysis a baffle length of 150 mm was selected as it offers the best straylight rejection while also respecting volumetric constraints.

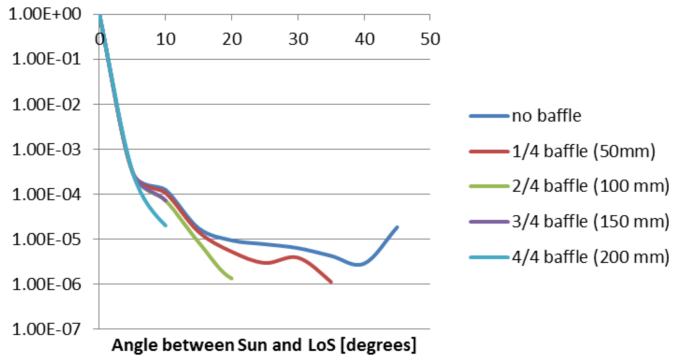

Figure 1.6: Preliminary straylight results

Two identical 1024 × 1024 CCD detectors (CCD201-20) are used for the two focal plane assemblies and each of them is coupled to TEC (thermo-electric cooler) to keep the temperature of the detector at a temperature of −20°C necessary to minimise dark current noise (thus maximizing the SNR).

Mechanical system design

The baseline is to use a 12 U cubesat structure with deployable solar arrays to accommodate all the components and the payload. At the moment due to the choice of mounting the baffle internally to the main structure (for higher compatibility for launch opportunities) there are volume criticalities that have to be solved by optimizing the trajectory design to reduce the propellant tank volume.

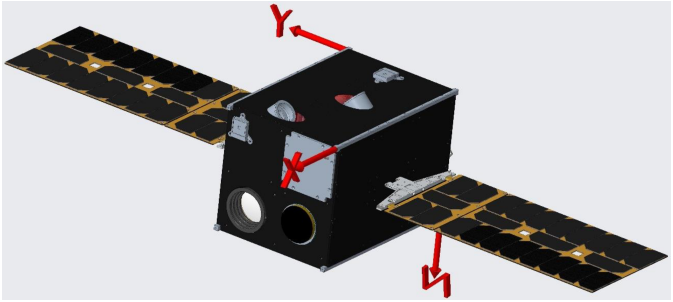

Figure 1.7: LUMIO external configuration

Electrical Power Subsystem (EPS)

The EPS is made of a power generation unit (two movable solar arrays), a power storage unit and a power distribution unit.
The Solar Array Drive Assembly (SADA) is made of two $1,5 \times 6$ U deployable solar panels, a deployment mechanism, a drive mechanism and a control unit. Deployable solar panels are necessary as body mounted solar panels would not generate enough power. The deployment mechanism selected is a Hold Down and Release (HDR) system due to its simplicity and low volume (a wire keeping the arrays closed is burned upon a signal received by the control unit). The drive mechanism is used to rotate independently the two solar arrays along the y body axis to maximize power generation. The control unit commands the HDR mechanism, the motors of the drive mechanism and the health status of the solar panels. To size the EPS, every operative mode of the satellite has been analysed considering which subsystems were active and the activity level of every component. The results are reported in Tab.(1.4).

Mode	Total [W]	Total with 20% margin [W]
Science	45.13	54.15
Prop. Heating	57.79	69.35
Transfer	46.80	56.16
Ranging	28.40	34.08
PL transmission	39.78	47.74
RW desaturation	36.04	43.24
Nominal Nav&Eng	6.56	7.87
Safe	30.97	37.17
Sleeping	0.00	0.00

Table 1.4: Modes power consumption

When computing the power generated from solar arrays it must be kept in mind its oscillatory behaviour. Considering an average solar flux of $1360\, W/m^2$ at 1 AU, the periodicity of the halo orbit (higher frequency) and the Earth-Moon system orbit around the Sun (lower frequency) cause an oscillation in the available power. This behaviour is clearly visible in Fig.(1.8) where the orange line represents the required power in science mode. In the time periods where $P_{generated} < P_{available}$, a reduced science cycle is performed with lower quality scientific output because not even the batteries can make up for this power deficiency for such an extended amount of time.

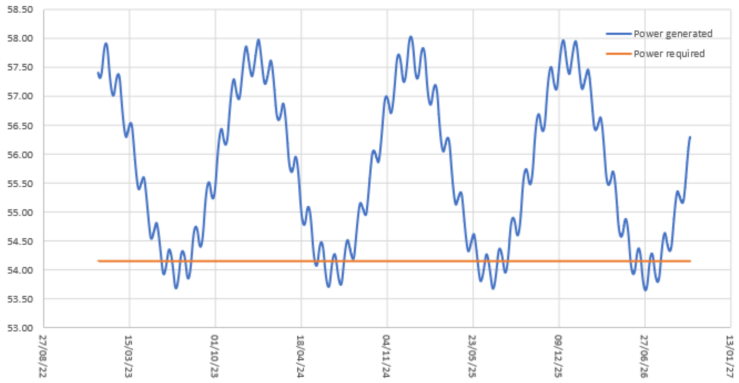

Figure 1.8: Preliminary power balance analysis

The function of the Battery Unit (BU) on LUMIO is to provide power during eclipses, absorb excess power generated and supply additional power during peak consumption periods. The satellite will use two lithium-ion battery packs for a total capacity of 25600 mAh. The conditioning unit enables peak power tracking power generation logic and the distribution unit allows to control how much power is given from the EPS to the various subsystems.

Command and data handling subsystem

This is the *brain* of the spacecraft, its roles are: gathering and storing telemetry (for health status) to be sent to Earth, sending real time housekeeping data, receiving data and commands from ground, controlling all the subsystems and implementing Failure Detection Isolation and Recovery (FDIR). The selected hardware is the ISISpace onboard computer with its flight software built around it for optimal performances.

Communication subsystem design

The tasks of this subsystem are: sending telemetry and receiving commands, transferring PL data, ranging and tracking for navigation. Two options were studied and traded off:

1. Inter-Satellite link (ISL): uses a relay satellite to send data to Earth. In this case the satellite used as bridge would be the SSTL lunar pathfinder with the possibility to use UHF and S-band frequencies. UHF has been excluded because of the possible interferences caused by the presence of hydrogen on Moon's surface that may cause high redshift, the only solution possible for ISL is to use the S-band. This configuration would allow datarates in the order of $0.5 - 2\,kbps$ thus it cannot be exploited for navigation purposes.

2. Direct to Earth (DTE): in this case, being the distance with the satellite always lower than 2 million km, near Earth communication bands were considered: X-band up/downlink, X-band downlink S-band uplink, S-band up/downlink. Considering also the ground stations available for communication the X-band up/downlink solution was considered optimal.

After performing a trade-off between ISL and DTE both were selected to be used in different situations. ISL will be used for commanding the satellite in nominal situations due to the lower power required. DTE will be used for PL downlink and ranging & tracking in nominal conditions due to better link budget and the possibility to use multiple channels. It will also be used for emergency operations.

Attitude Dynamics Control System (ADCS)

Due to the mission architecture, the best attitude control strategy to satisfy Moon pointing requirements is to align the pitch axis with the Sat-Moon-Sun plane (visible in Fig.(1.3)) then, to maximize power generation it is necessary to have rotating solar panels.
The sensor suite for LUMIO is made of: one fine Sun-sensors on each face for a total of six (MAUS CubesatSun sensor from Lens R&D), 2 star trackers (AURIGA Startracker by Sodern) and one inertial measurement unit (ISISpace IMU). The actuator mounted on the satellite are: 4 reaction wheels (ISISpace RW25 SW50) in a 3-axis and diagonal configuration for redundancy and a Reaction Control System (RCS). The RCS together with the main propulsion are still being optimized to minimize the propellant tank size due to volume budget criticalities.

Thermal control system

After defining minimum and maximum temperature for inner and outer environment of the satellite, the two worst case scenarios (hot and cold) identified during the environmental analysis can be studied to design an optical TCS. Being the hot and cold case conditions quite similar and, due to the nature of the mission it was considered reasonable and convenient to use completely passive control by selecting proper surface coatings/finishes and by properly orienting the spacecraft. More detailed multi-node analyses will be performed in phase B to identify eventual residual critical aspects and to ensure that each single component remains in its correct temperature range (operational/survival) at every time.

On Board Payload Data Processing system

An estimation of the total amount of data collected by LUMIO can be made by considering 1024×1024 image size for each of the 2 detectors and a 14-bit pixel depth. This means that each image is 3,67 MB; considering the 15 fps of the LUMIO-Cam, the data collected amounts to 4,76 TB/day, 69,0 TB for an average 14.5 day scientific cycle and 828 TB for the entire mission duration. When considering LUMIO's downlink capability of $\simeq$ 5 MB/day, it is clear that the amount of raw data is not manageable. The OBPDP is then fundamental to reduce the amount of informations to be transmitted; the first task of this system is in fact of selecting only scientifically relevant data for transmission and secondly to occasionally store full images to perform the autonomous navigation experiment during the Nav&Eng phase.

Since the architecture of LUMIO's detectors is very similar to that of NELIOTA, the algorithm used in the OBPDP system for flash identification is an adaptation and simplification of the one used in NELIOTA. To reduce the amount of data, the software automatically detects flashes in the images and only stores scientifically relevant portions of them. The first step in the algorithm is to identify images containing a flash and only considering the 5 frames around the flash (2 frames before, 2 after and the flash frame itself). The second step is cutting and storing only a 50×50 pixel tile around each detected flash for all the five frames previously selected. This procedure allows to reduce the amount of data from 4,76 TB/day to 1,36 TB/day considering $\simeq$31 flashes/day.

To be able to detect a flah it is first necessary to define what a flash actually is: *a flash is an instantaneous rise in the intensity of the signal at the time of the impact followed by an exponential decay (dissipation) back to the intensity level prior to the impact (background level).* It is also useful to define what is not a flash: all intensity drops or rapid intensity increase not followed by exponential decay. To prevent false positive, for a flash to be considered such it is required that it appears simultaneously on both detectors in pixels corresponding to the same viewing direction.

The algorithm simplification previously mentioned is necessary to be able to perform every operation directly on board of the spacecraft and consists in analysing first only the NIR channel (because highest SNR is expected here) looking for possible flashes. If a considerable brightness fluctuation is detected, the VIS channel is taken into consideration; in this case however only the pixel area around the suspected flash is considered instead of the entire picture. This procedure nearly halves the computational load without altering flash detection performances.

2 | Heat transfer theory

The scope of this chapter is that of revising the theory of all the fundamental heat transfer phenomena together with the main models used to describe and analyse them focusing only on the aspects relevant for the analysis to be performed on the LUMIO-Cam.

2.1. Conservation of energy

Being heat transfer closely related to general thermodynamics, the first law of thermodynamics (the conservation of energy principle) represents an essential tool. This principle states that the total energy of a system must be conserved and the only way in which it can change is if it crosses the boundaries of the system itself. For a closed system as the one of Fig.(2.1) (region of fixed mass) the only means by which energy can cross its boundaries is by heat transfer or if work is done by/on the system. Expressing this principle in a mathematical way:

$$\Delta E_{st}^{TOT} = Q - W \tag{2.1}$$

ΔE_{st}^{TOT} is the change in the total energy stored in the system, heat (Q) is positive by convention if entering the system and work (W) is positive if performed by the system. The first law of thermodynamics addresses the total energy which is made of three contributions: internal energy (U), kinetic energy and potential energy (together the last two make the mechanical energy). Internal energy can be further subdivided in: thermal,

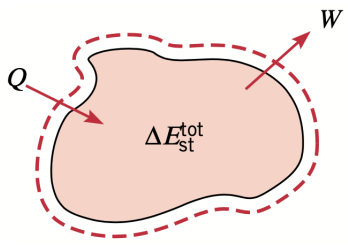

Figure 2.1: Conservation of energy for a closed system

chemical and nuclear energy thus is it fundamental to remember that the summation of mechanical energy and thermal energy may not be constant because there can be conversion from other form if internal energy to thermal.
Considering a time interval (Δt) the increase in the amount of thermal and mechanical energy stored in the control volume must equal the amount of thermal and mechanical energy that enters the control volume, minus the amount of thermal and mechanical energy that leaves the control volume, plus the amount of thermal energy that is generated within the control volume. In a mathematical way:

$$\Delta E_{st} = E_{in} - E_{out} + E_{gen} \tag{2.2}$$

Since the energy conservation principle must be valid at any time instant it is possible to reformulate the previous statement considering rates, the previous equation then becomes:

$$\dot{E}_{st} = \dot{E}_{in} - \dot{E}_{out} + \dot{E}_{gen} \tag{2.3}$$

The energy generation term (E_g) associated to internal energy transformation is a volumetric phenomenon meaning that its magnitude is proportional to the volume of the system. Inflow and outflow terms are instead surface phenomena thus they are proportional to surface are of the system.
The solution of heat transfer problems often requires the application of the first principle of thermodynamics. The first step in using this powerful tool is the identification of the appropriate control volume, secondly Eq.(2.2) and Eq.(2.3) are used to perform a time interval or rate analysis solution respectively. This choice depends on the objective of the solution and the information known about the problem. Finally to compute the solution the proper heat transfer equations are substituted.

2.2. Conduction

Conduction is the basic heat transfer mechanism in all solid materials. The governing equation of conduction is known as *Fourier law* and it was determined experimentally from multiple observations. Consider the simple case of a rod with adiabatic lateral surface and a temperature difference ΔT between the two bases (Fig.(2.2)). Taking as independent variables ΔT, Δx (length of the rod $[m]$), A (cross sectional area $[m^2]$) it was observed a dependency of the heat rate from these variables. Changing the material of the rod also influenced the heat rate across the two surfaces thus a material specific

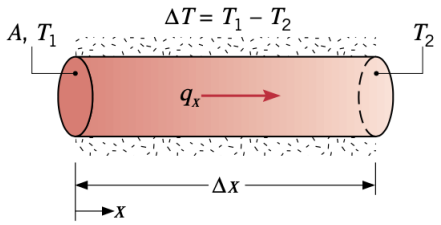

Figure 2.2: 1D axial conduction in a rod

parameter (thermal conductivity) has been introduced; the proportionality law can be expressed as $q_x \propto kA\frac{\Delta T}{\Delta x}$. Finally, the Fourier law can be derived by considering the heat flux and evaluating the expression for $\Delta x \to 0$:

$$q''_x = -k\frac{dT}{dx} \tag{2.4}$$

where the minus sign is due to the heat moving from hotter zones to colder ones. From Eq.(2.4) it is clear that heat flux is directional, in particular in this case it is perpendicular to the cross sectional area. In a more general 3-D case, the flux is normal to isothermal surfaces and the equation becomes:

$$q''_x = -k\nabla T = -k\left(\frac{\delta T}{\delta x} + \frac{\delta T}{\delta y} + \frac{\delta T}{\delta z}\right) \tag{2.5}$$

In any case to be able to use Fourier equation, the knowledge of k (defined ad $k_x = -\frac{q''_x}{\delta T/\delta x}$) is necessary. In general cases, the thermal conductivity can depend on the heat direction ($k = k(x, y, z) = k_x\hat{i} + k_y\hat{j} + k_z\hat{k}$) but in many cases the material can be considered isotropic which means $k_x = k_y = k_z \equiv k$. Values of k for most materials can be found in the literature and have been computed experimentally.

2.2.1. Heat diffusion equation

Of great interest in many heat conduction analyses is to determine the temperature distribution in the object being analysed. This objective can be achieved by applying the energy conservation principle described in the previous section.
Consider a homogeneous medium with a cartesian reference frame; the temperature distribution can be expressed as $T = T(x, y, z)$ end the infinitesimal control volume can be

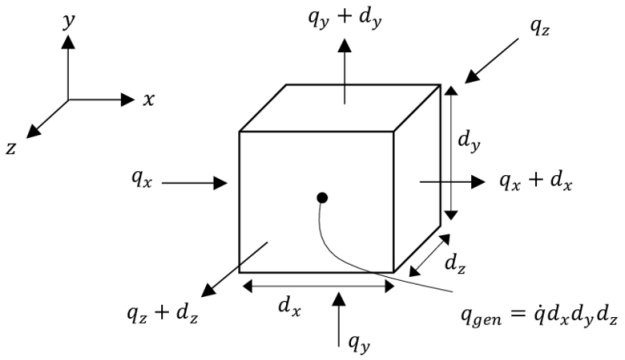

Figure 2.3: Infinitesimal control volume in cartesian coordinates

computed as $dV = dx\,dy\,dz$ (Fig.(2.3)). Assuming the presence of a temperature gradient across the volume, there will be heat transfer across the control surfaces. The following equations express how the heat changes with respect to a change of position of the control surface.

$$\begin{cases} q_{x+dx} = q_x + \dfrac{\delta q_x}{\delta x} dx \\ q_{y+dy} = q_y + \dfrac{\delta q_y}{\delta y} dy \\ q_{z+dz} = q_z + \dfrac{\delta q_z}{\delta z} dz \end{cases} \tag{2.6}$$

Considering also the presence of internal energy generation and storage in the control volume

$$\begin{cases} \dot{E}_g = \dot{q}\,dx\,dy\,dz \\ \dot{E}_{st} = \rho c_p \dfrac{\delta T}{\delta t} dx\,dy\,dz \end{cases} \tag{2.7}$$

Applying the conservation of energy principle ($\dot{E}_{in} + \dot{E}_g - \dot{E}_{out} = \dot{E}_{st}$) where the energy entering and exiting the control volume are respectively $\dot{E}_{in} = q_x + q_y + q_z$, $\dot{E}_{out} = q_{x+dx} + q_{y+dy} + q_{z+dz}$ and substituting from Eq.(2.6) the result is:

$$-\frac{\delta q_x}{\delta x} dx - \frac{\delta q_y}{\delta y} dy - \frac{\delta q_z}{\delta z} dz + \dot{q}\,dx\,dy\,dz = \rho c_p \frac{\delta T}{\delta t} dx\,dy\,dz \tag{2.8}$$

By remembering that $q_x = -k\dfrac{\delta T}{\delta x} dy\,dz$ (similar for q_y and q_z) and simplifying common

terms, the previous equation can be rewritten in a more compact form as:

$$\nabla(k\nabla T) + \dot{q} = \rho c_p \frac{\delta T}{\delta t} \tag{2.9}$$

Solving this differential equation (second order in space and first order in time), it is possible to retrieve the temperature distribution of the object at any time instant.
Note that there are many coordinate systems that are often more appropriate than the cartesian one such as the cylindrical and the spherical reference systems.

2.2.2. Boundary and initial conditions

To solve the heat equation some boundary and, if the problem is time dependent, initial conditions are necessary (two boundary conditions and one initial condition as the equation is second order in space and first order in time). With regard to boundary conditions, considering an arbitrary boundary position $\hat{x}$, there are three main possibilities:

1. Constant temperature: $T(\hat{x}, t) = T$.
2. Finite heat flux: $-k\frac{\delta T}{\delta x}\Big|_{x=\hat{x}} = q$. If the surface is adiabatic $q = 0$.
3. Convention and/or radiation: $-k\frac{\delta T}{\delta x}\Big|_{x=\hat{x}} = q_{conv/rad}$

Initial conditions will be analysed later when considering transient solutions.

2.2.3. Steady state solution

To start solving the heat diffusion equation it is best to first consider *steady state* problems (those cases in which the solution is not time dependent). If some conditions are verified, the overall problem can sometimes be greatly simplified by making some assumptions. The simplest case is verified when the conduction can be assumed to be mono-dimensional. In this case the problem is described by a single ordinary differential equation that can simply be solved by integration and application of boundary conditions. When the problem is bi-dimensional the governing equations are partial differential equations thus the solution is much more complex. However the solution can still be computed analytically with the separation of variable technique if the boundary conditions are simple enough. Whenever the boundary condition are too complex or the problem is thee-dimensional, numerical methods are the only viable option to compute the solution.

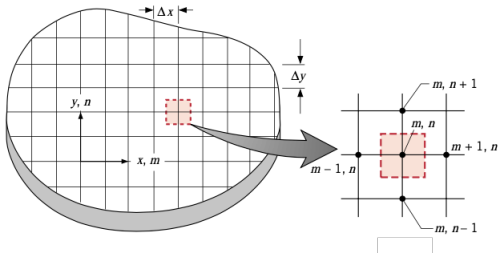

Figure 2.4: Finite difference nodal subdivision

Numerical method: finite difference method

The most suited numerical method for thermal application is the finite difference method. Numerical methods allow to compute an approximate solution only at discrete points of the domain, called *nodes*. The overall domain is subdivided in smaller sections each with a node in its center concentrating there all the thermophysical properties of the area. An example of this nodal network is shown in Fig.(2.4).
At this point, an appropriate energy conservation equation in the finite difference form must be written for each node. The resulting set of equations can be solved simultaneously to find the temperature of all the nodes.
The application of finite difference approximation to thermal case is as follows:

$$\left.\frac{\delta^2 T}{\delta x^2}\right|_{m,n} \approx \frac{\delta T/\delta x|_{m+1/2,n} - \delta T/\delta x|_{m-1/2,n}}{\Delta x} \tag{2.10}$$

with

$$\begin{cases} \left.\dfrac{\delta T}{\delta x}\right|_{m+1/2,n} \approx \dfrac{\delta T/\delta x|_{m+1,n} - \delta T/\delta x|_{m,n}}{\Delta x} \\ \left.\dfrac{\delta T}{\delta x}\right|_{m-1/2,n} \approx \dfrac{\delta T/\delta x|_{m,n} - \delta T/\delta x|_{m-1,n}}{\Delta x} \end{cases} \tag{2.11}$$

Substituting Eq.(2.11) into Eq.(2.10) (with an analogous procedure along y axis):

$$\begin{cases} \left.\dfrac{\delta^2 T}{\delta x^2}\right|_{m,n} \approx \dfrac{T|_{m+1,n} + T|_{m-1,n} - 2T|_{m,n}}{\Delta x^2} \\ \left.\dfrac{\delta^2 T}{\delta y^2}\right|_{m,n} \approx \dfrac{T|_{m,n+1} + T|_{m,n-1} - 2T|_{m,n}}{\Delta y^2} \end{cases} \tag{2.12}$$

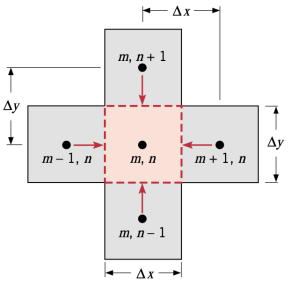

Figure 2.5: Internal nodes interaction

Considering any internal node of a steady state system with constant conductivity and no internal heat generation, the heat equation approximated using a network such that $\Delta x = \Delta y$ becomes:

$$\nabla^2(T) = 0 \approx T_{m,n+1} + T_{m,n-1} + T_{m+1,n} + T_{m,n-1} - 4T_{m,n} = 0 \tag{2.13}$$

Very often the direct application of FD approximation to the heat equation is not convenient due to the problem complexity. A much better method is the *energy balance method* that allows to analyze problems with different materials, internal power generation, complex geometries and boundary conditions. This method simply consists of applying the conservation of energy principle to every nodal region. With this logic, the real direction of the heat flow is often unknown thus all flow is considered entering the volume. This is clearly not physically possible but if computations are performed consistently with this hypothesis, the end result will be correct. Considering for example a steady state system with internal heat generation; the energy balance is:

$$\dot{E}_{in} + \dot{E}_g = 0 \tag{2.14}$$

Applying this equation to the node (m,n) in Fig.(2.5), the result is:

$$\sum_{i=1}^{4} q_{(i)\to(m,n)} + \dot{q}(\Delta x \Delta y) = 0 \tag{2.15}$$

A fundamental assumption in the finite difference method is that heat travels from a node to another only parallel to the axes of the grid; this assumption allows the use of simplified Fourier law ($q = kA\Delta T/d$) and thermal resistance concept. For example, considering nodes (m,n) and $(m+1,n)$:

$$q_{(m-1,n)\to(m,n)} = k\Delta y \frac{T_{m-1,n} - T_{m,n}}{\Delta x} = \frac{\Delta T}{R} \tag{2.16}$$

and analogous for the other three nodes. Assuming $\Delta x = \Delta y$:

$$T_{m,n+1} + T_{m,n-1} + T_{m+1,n} + T_{m-1,n} - 4T_{m,n} + \frac{\dot{q}\Delta x^2}{k} = 0 \tag{2.17}$$

The previous equation is valid for every internal node of the system. If the geometry is changed, the energy balance components can be easily re-formulated according to the new geometry or boundary conditions.
The application of thermal resistance concept is particularly helpful whenever the system to be analyzed has an interface between two different materials as the contact resistance can be simply put in series with those of the two solids.
After obtaining the system of approximate heat equations, it must be solved to find the nodal temperatures. The system is made of linear equations and it can be solved with many direct or indirect (iterative) numerical methods.
A good example of a direct method is the *matrix inversion* method. The equations can be reformulated to express the system in matrix notation as: $A\,T = C$ where A and C are respectively a matrix and a vector of known coefficients and T is the vector of unknown nodal temperatures. The solution of this problem can be computed as $T = A^{-1}C$; this operation can easily be performed by a computer (depending on the number of unknowns).
An example of iterative method can be the Gauss-Seidel iteration. The steps are:

1. Reorder the equations so that the diagonal elements are greater than the others on the same line. If this can be done for every equation then the system is diagonally dominant and the rate of convergence of the method is increased.
2. Rewrite each equation so that the diagonal temperature unknown is explicit.
3. Assume an initial value for each unknown temperature.
4. Start iterating the value of each temperature.
5. Computations are terminated when the difference of two consecutive iterations is lower than the desired accuracy (ϵ), $|T_i^{(k)} - T_i^{(k+1)}| < \epsilon$.

It is important to remember that the finite difference method is an approximation which accuracy depends on the meshing (Δx, Δy) size. If the accuracy is not satisfactory the meshing can be refined until the results of the analysis become independent from their value thus effectively eliminating the approximation effect.

2.2.4. Transient solution

When the problem is time dependent an additional complexity level is added to the solution process. The procedures used to evaluate the temperature dependency from time are different and derive from the hypothesis of the problem. For example, if conduction inside the solid is much faster than the heat exchange from the solid to the environment, the lumped parameter capacitance approach can be used to solve the problem in few steps. When the previous hypothesis is not verified but the conduction problem can be assumed mono-directional, the finite or semi-infinite solid approximation can be used again with great simplicity. In every other more complex problem, the use of finite difference approximation is necessary.

Finite difference method

The concepts introduced in the previous section can be easily extended to the solution process of transient cases. To show the application of finite difference approximation to a transient analysis, a simple 2-D example with constant properties and no internal heat generation can be considered. The general heat equation is:

$$\frac{\rho c_p}{k}\frac{\delta T}{\delta t} = \frac{\delta^2 T}{\delta x^2} + \frac{\delta^2 T}{\delta y^2} \tag{2.18}$$

With respect to space discretization, the central difference technique will be used again with subscripts *m,n*. To discretize the equation in time, superscript p is used to indicate the time instant of computation:

$$\left.\frac{\delta T}{\delta t}\right|_{m,n} \approx \frac{T^{p+1}_{m,n} - T^{p}_{m,n}}{\Delta t} \tag{2.19}$$

Using the finite difference approximation, the solution is approximated only at discrete instants of time. Substituting Eq.(2.19) into the heat equation and remembering the spatial discretization of Eq.(2.12) applied at the present time instant $T^{p}_{m,n}$, it is possible to compute the finite difference approximation of the transient heat equation:

$$\frac{\rho c_p}{k}\frac{T^{p+1}_{m,n} - T^{p}_{m,n}}{\Delta t} = \frac{T^{p}_{m+1,n} + T^{p}_{m-1,n} - 2T^{p}_{m,n}}{\Delta x^2} + \frac{T^{p}_{m,n+1} + T^{p}_{m,n-1} - 2T^{p}_{m,n}}{\Delta y^2} \tag{2.20}$$

Eq.(2.20) is in the *explicit* form because all the temperatures with the superscript p are

known and the temperature value at the next step depends only on these. Solving for T^{p+1} and assuming $\Delta x = \Delta y$ for simplicity:

$$T^{p+1}_{m,n} = Fo(T^{p}_{m+1,n} + T^{p}_{m-1,n} + T^{p}_{m,n+1} + T^{p}_{m,n-1}) + (1 - 4Fo)T^{p}_{m,n} \tag{2.21}$$

with $Fo = k\Delta T/\rho c_p \Delta x^2$ (finite difference equivalent of Fourier number). The solution is quite simple; starting from the initial conditions given for $p = 0$, the problem is solved by marching forward in time. The accuracy of the explicit method solution is improved by lowering the values of Δx and Δt but, the smaller they get, the more the computational cost increases. Usually the first step is to establish the optimal value of Δx by performing a trade-off analysis between accuracy and computational cost, after that the value of Δt is determined. Since explicit methods are *conditionally stable* however, the value of the time-step shall comply with stability requirements of the solution to avoid divergence of the solution. For most thermal problems the stability criterion is that the coefficient multiplying the temperature of the node of interest at the previous time step must be greater than zero. Considering for example Eq.(2.21) this leads to:

$$(1 - 4Fo) \geq 0 \rightarrow Fo \leq \frac{1}{4} \rightarrow \Delta t \leq \frac{\Delta x^2 \rho c_p}{4k} \tag{2.22}$$

Obviously the previous condition is not general as the stability requirement is specific of the heat equation which depends on the node itself (boundary conditions, internal generation, ...). Whenever there is more than one condition, only the most stringent one can ensure overall stability of the solution.
Often the stability requirements lead to very small values of Δt which slow down the computation to unacceptable limits. When this happens it is much more convenient to use *implicit* methods. In this case the temperature value of a node at the time $p + 1$ depends also on the temperature values of the neighboring nodes at $p + 1$. The equation is:

$$\frac{\rho c_p}{k}\frac{T^{p+1}_{m,n} - T^{p}_{m,n}}{\Delta t} = \frac{T^{p+1}_{m+1,n} + T^{p+1}_{m-1,n} - 2T^{p+1}_{m,n}}{\Delta x^2} + \frac{T^{p+1}_{m,n+1} + T^{p+1}_{m,n-1} - 2T^{p+1}_{m,n}}{\Delta y^2} \tag{2.23}$$

Assuming again $\Delta x = \Delta y$ the heat equation becomes:

$$(1 + 4Fo)T^{p+1}_{m,n} - Fo(T^{p+1}_{m+1,n} + T^{p+1}_{m-1,n} + T^{p+1}_{m,n+1} + T^{p+1}_{m,n-1}) = T^{p}_{m,n} \tag{2.24}$$

The solution of Eq.(2.24) is not immediate as the unknown ($T_{m,n}^{p+1}$) depends on values that are unknown themselves (the temperature of adjacent nodes at $p+1$). This means that the problem can be solved only if the equations of all nodes are solved simultaneously; this is possible by using the Gauss-Seidel method or the matrix inversion method. This solution process is more computationally expensive than explicit methods but the big advantage is that implicit methods are *unconditionally* stable thus enabling the use of higher Δt which allows faster computation. The time-step value however shall always be kept low enough to ensure accuracy and especially to ensure that the results of the solution are independent from ulterior reduction of its value.

2.3. Radiation

This kind of heat transfer mechanism does not require the presence of a medium to happen; in fact it is mot efficient in vacuum. Radiation is a surface phenomenon and its energy transport can be attributed both to photons or to electro-magnetic waves. In any case it is standard practice to treat radiation using wave properties (frequency and wavelength).

2.3.1. Rad properties

The fundamental radiation properties necessary to study the phenomenon will be presented in this section.
The most appropriate coordinate system to treat radiation is the spherical one, it is important to recall the definition of a differential solid angle as the one shown in Fig.(2.6): $d\omega = \dfrac{dA_n}{r^2}$.

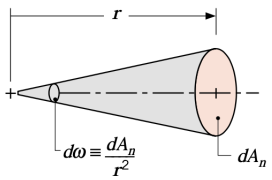

Figure 2.6: Infinitesimal solid angle

- **Spectral intensity**: $I_{\lambda,e}(\lambda,\theta,\phi)$ defined as *"rate at which radiant energy is emitted at wavelength λ in the direction ($\theta\,\phi$) per unit are of emitting surface perpendicular to this direction, per unit solid angle about this direction and per unit wavelength interval $d\lambda$ about λ"*. From the spectral emissivity the flux of emitted energy can

be computed.

- **Spectral hemispherical emissive power**: $E_\lambda(\lambda)$ is the directional average of the flux but it is till wavelength dependent. The total emissive power can be computed integrating over all wavelengths.
- **Irradiation**: $G_\lambda(\lambda)$ defined as *"rate at which radiant energy of wavelength λ is incident from the direction (θ, ϕ) per unit area of intercepting surface normal to this direction, per unit solid angle about this direction and per unit wavelength interval $d\lambda$ about λ"*. Again, the total irradiation can be computed integrating for all wavelengths.
- **Radiosity**: $J_\lambda(\lambda)$ accounts for all radiant energy leaving the surface (emitted and reflected).

2.3.2. Black-body radiation

To evaluate the properties defined above, it is necessary to introduce the concept of *black body* which is an object with the following characteristics:

- It absorbs all incident radiation independent of its wavelength and direction.
- For and defined temperature and wavelength, no surface can emit more radiation than a black body.
- It is by definition a diffuse emitter.

It is fundamental to know that perfect black bodies do not exist even though they can be well approximated by some surfaces and coatings. The best approximation of a black body is a cavity with uniform internal temperature.
Some important laws for a black body have been determined. The spectral intensity of a black body can be computed as:

$$I_{\lambda,b}(\lambda, T) = \frac{2\,h\,c_0^2}{\lambda^5\,[exp(h\,c_0/k\,\lambda\,T) - 1]} \tag{2.25}$$

Where h is the universal Planck constant, k is the universal Boltzmann constant and c_0 is the speed of light in vacuum. The spectral hemispherical and total emissive power of a black body are:

$$\begin{cases} E_{\lambda,b}(\lambda,T) = \pi I_{\lambda,b}(\lambda,T) \\ E_b(T) = \int_o^\infty E_b(\lambda,T)d\lambda = \sigma T^4 \end{cases} \tag{2.26}$$

2.3.3. Real surfaces

After defining a black body, it is possible to define the properties of real bodies. The first property is *emissivity* which is defined as the ratio between the energy emitted by a real surface divided by the energy emitted by a blackbody at the same temperature. It can be interpreted as a sort of temperature dependant emission efficiency of real objects and can be defined for directional, hemispherical or total cases ($\varepsilon = E_{real}/E_{blacbody}$).
Other important properties of a real surface are the *absorptivity* (α), *reflectivity* (ρ) and *transmissivity* (τ). These properties express the percentage of energy that is respectively absorbed, reflected or transmitted by a body compared to the total incident radiation hitting that body. When total irradiation (G) hits the surface, it is split in three contributions:

$$G_\lambda = G_{\lambda,abs} + G_{\lambda,ref} + G_{\lambda,tr} \tag{2.27}$$

In the majority of cases however, the impact surface can be considered opaque thus $G_{\lambda,tr} = 0$.
A fundamental property regarding these three parameters is: $\alpha + \rho + \tau = 1$ for semi-transparent and $\alpha + \rho = 1$ for opaque surfaces.

Grey surface

A grey surface is characterized by having $\alpha = \varepsilon$. Real surfaces must satisfy some conditions to be defined as grey. First, one of these two conditions must be satisfied:

- Irradiation is diffuse (it does not depend on the direction).
- Surface is diffuse (optical properties do not depend on the direction).

Assuming one of the two conditions to be true, the following step is to verify that either: irradiation is caused by black body emission (such that $G_\lambda(\lambda) = E_{\lambda,b}(\lambda,T)$ and $G = E_b(T)$) or the surfaces optical properties do not depend on the wavelength.
Being the first condition a very strong assumption, the focus is on the second one.
Note that absorptivity of almost every material strongly depends on the spectral distribution of the irradiation ($\alpha_\lambda(\lambda)$) while the emissivity is independent. Thus in general it

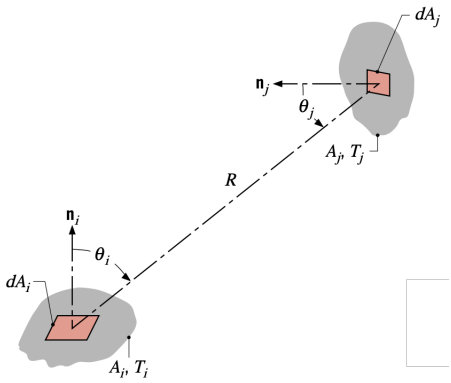

Figure 2.7: View factor between infinitesimal surfaces

cannot be stated that $\varepsilon = \alpha$. It is however possible to define for every surface a wavelength interval in which the absorptivity value is constant, in that region then it is possible to assume the absorption and emission properties to be equal leading to the definition of a diffuse, gray surface.

2.3.4. Radiation exchange between surfaces

After introducing the governing principle of radiation, the next step is to study how heat can be exchanged between surfaces. A fundamental parameter when studying radiative interaction between surfaces is the so called *view factor* (F_{ij}) which is defined as the fraction of radiation leaving surface i that is intercepted by surface j.
Considering two elemental surfaces dA_i, dA_j at a distance R which direction forms polar angles $\theta_i\, \theta_j$ with the normal to the surfaces (Fig.(2.7)). The rate at which radiation from dA_i is intercepted by dA_j is:

$$dq_{i\to j} = I_{e+r,i} cos\theta_i \, dA_i d\omega_{j\to i} \tag{2.28}$$

Since $d\omega_{j\to i} = cos\theta_j \, dA_j / R^2$ and assuming surface i to be diffuse:

$$dq_{i\to j} = J_i \frac{cos\theta_i cos\,\theta_j}{\pi R^2} dA_i dA_j \to q_{i\to j} = \int_{A_i}\int_{A_j} dq_{i\to j} \tag{2.29}$$

The view factor between diffuse emitter and reflector surfaces with uniform radiosity is then:

$$F_{i,j} = \frac{q_{ij}}{A_i J_i} \tag{2.30}$$

Two important properties of the view factors are the reciprocity rule ($F_{ij}A_i = F_{ji}A_j$) and the summation rule in an enclosure ($\sum_{j=1}^{N} F_{ij} = 1$ where N is the number of surfaces in the enclosure).
To simplify the analysis of net radiation exchange, some assumptions are made: surfaces will be considered gray opaque, diffuse and isothermal with uniform radiosity and irradiation. Considering a surface i of an enclosure, and defining q_i as the net rate at which radiation leaves the surface as effect of radiation interactions. It is also the rate at which heat would have to be transferred to the surface by other means to maintain a constant temperature.

$$q_i = A_i(J_i - G_i) \tag{2.31}$$

Since $J_i = E_i + \rho_i G_i$

$$q_i = A_i(E_i + (\rho_i - 1)G_i) \tag{2.32}$$

Equating the two previous formulas and remembering $(\rho_i - 1) = -\alpha_i = -\varepsilon_i$, $E_i = \varepsilon_i E_{i,b}$:

$$J_i = \varepsilon_i E_{i,b} + (1 - \varepsilon_i)G_i \rightarrow G_i = \frac{J_i}{\varepsilon_i E_{i,b} + (1 - \varepsilon_i)} \tag{2.33}$$

Substituting this result in the first equation:

$$q_i = \frac{E_{i,b} - J_i}{(1 - \varepsilon_i)/\varepsilon_i A_i} \tag{2.34}$$

This formulation is very useful to exploit a similarity to an electrical network where the potential would be $E_{i,b} - J_i$ and the radiative resistance is $(1 - \varepsilon_i)/\varepsilon_i A_i$. It must be noted that to use Eq.(2.34), the surface radiosity (J_i) needs to be known. It is thus necessary to consider the radiation exchange with the other surfaces of the enclosure. The irradiation of surface i can be expressed in relation to other surfaces radiosities as:

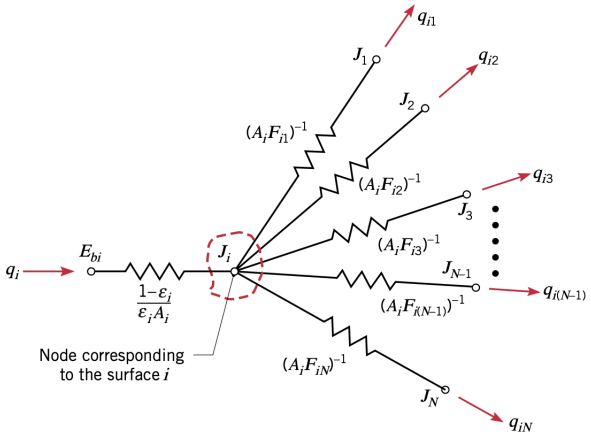

Figure 2.8: Network similarity

$$A_i G_i = \sum_{j=1}^{N} F_{ji} A_j J_j = \sum_{j=1}^{N} F_{ij} A_i J_j \tag{2.35}$$

Where the reciprocity rule has been exploited. Substituting the previous relation in Eq.(2.31) and applying the summation rule, it is obtained:

$$q_i = A_i(J_i - \sum_{j=1}^{N} F_{ij} J_j) = \sum_{j=1}^{N} A_i F_{ij}(J_i - J_j) = \sum_{j=1}^{N} q_{ij} \tag{2.36}$$

Performing again a network similarity, the driving potential is $J_i - J_j$ and the resistance is $(A_i F_{ij})^{-1}$. Imposing Eq.(2.34) equal to Eq.(2.36), the complete network representation is obtained (Fig.(2.8)).

Two surface radiation

To start applying the previous concepts to real cases, the simplest example is an enclosure comprising only two surfaces, in this configuration $q_1 = -q_2 = q_{12}$. Exploiting the network similarity of Fig.(2.9), the equations are:

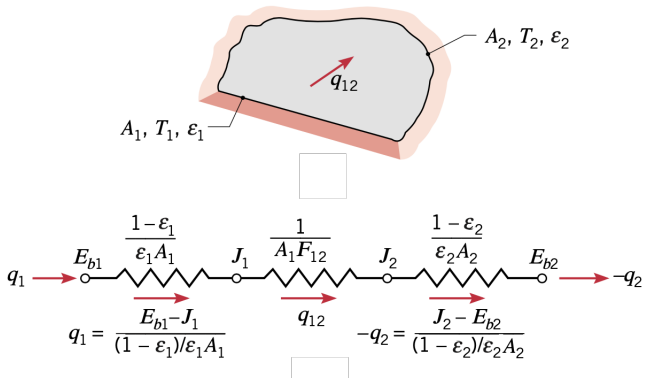

Figure 2.9: Two surface cavity

$$\begin{cases} q_1 = \dfrac{E_{b,1} - J_1}{(1-\varepsilon_1)/\varepsilon_1 A_1} \\ q_{12} = \dfrac{J_,1 - J_2}{(A_1 F_{12})^{-1}} \\ -q_2 = \dfrac{J_2 - E_{b,2}}{(1-\varepsilon_2)/\varepsilon_2 A_2} \end{cases} \tag{2.37}$$

Exploiting the series equivalent resistance:

$$q_{12} = q_1 = -q_2 = \frac{\sigma(T_1^4 - T_2^4)}{\dfrac{1-\varepsilon_1}{\varepsilon_1 A_1} + \dfrac{1}{A_1 F_{12}} + \dfrac{1-\varepsilon_2}{\varepsilon_2 A_2}} \tag{2.38}$$

2.4. Conclusions

Up to this point, conduction and radiation have been treated separately but in the application of interest for this thesis they will be present simultaneously acting on the system. The main difficulty in building an equivalent circuit considering both conduction and radiation together is that the first mechanism is proportional to a linear temperature difference ΔT while radiation uses a difference between temperatures elevated to the fourth power as seen in Eq.(2.38). Thanks to modern software however this ulterior complication can be managed easily.

3 | Modeling on Thermal Desktop

Thermal Desktop is an add-on of AUTOCAD developed by CR-Tech to build thermal models, analyse them and post process the results. It is a very complete and complex software with many functionalities which allows to analyse all kinds of thermal energy exchange (conduction, radiation and convection). In this chapter only the most important aspects to reach the goal of the thesis will be briefly covered.

3.1. General workflow

There is a common logic behind the generation of almost any thermal model in Thermal Desktop:

1. Create the file with appropriate settings and units (SI units).
2. Considering only conductive and radiative heat transfer two databases shall be created; one containing the thermo-physical properties of the materials used and the other with thermo-optical properties of materials and coatings.
3. Create the geometrical model using finite difference thin shells subdivided in nodes (diffusive/arithmetic/boundary).
4. Define heating environments (orbits) in which analyses will be performed.
5. Perform model checks (mass, area, active surfces, ecc).
6. Define the solution process based on the scope of the analysis (steady state, transitory, parametric, ecc).
7. Perform analysis and post-process the results.

For this thesis, being LUMIO an Italian project, metric units will be used.

3.1.1. Properties database

The *thermo-optical* properties database allows the definition of the necessary parameters in the visible and infra-red spectra (α, ε, τ, ρ, I). All the properties can be defined as constant values or as wavelength-dependent (except α that cannot have a wavelength dependency); additionally the absorptivity and emissivity can also be temperature-dependent. To distinguish the *begin-of-life* (BOL) and *end-of-life* (EOL) conditions in Thermal Desktop, two different strategies can be adopted:

1. The first method consists in creating two different optical properties databases, one for BOL and one for EOL. When defining analysis cases it is then possible to specify which database has to be used.

2. In the second method only one database is defined, within this database the optical property values that are affected by degradation can be defined using *symbols*. Symbols are used in Thermal Desktop as case dependent variables: a general value is defined for each symbol and then when defining a specific analysis case, the value can be over-written thus changing its value.

Both methods are equivalently valid, the choice on which to use depends on how many properties have to be defined and how many of them need to change value for different cases.
With regard to *thermo-optical* properties, it can store basic values as density, conductivity and specific heat but also advanced parameters as Young modulus, Poisson ratio, Seebeck coefficient and more. When defining the conductivity, multiple possibilities are available: it can be defined for a simple solid material, an aggregate or a laminate (all with different characteristics). Moreover, it is also possible to define it as directional, isotropic and temperature or pressure dependent. The specific heat can be constant or temperature/phase dependent.

3.1.2. Thermal model creation

When creating a thermal model of a real object it is convenient to exploit sub-models to better organize the overall process. This allows to define independent nodes numeration for each submodel, and can greatly simplify the solution process as entire submodels can be excluded/included in the solving process based on the different analysis cases.
Another very useful subdivision method is to define *radiation analysis groups*. The overall model often comprehends surfaces that will never exchange heat radiatively (for example exterior and interior surfaces). Since radiation exchange computation is a numerically

expensive process (Monte-Carlo ray tracing simulation), it is convenient to separate these groups to speed up the computation. An additional advantage is that for different radiation analysis groups, different radiation calculations can be performed, for example for exterior surfaces both environmental heat fluxes and radiative conductances are of interest while for interior surfaces only radiative conductances are computed to easy the solution. It is important to underline that radiation analysis group subdivision is totally unrelated to submodel subdivision and that a single surface can be in more than one radiation analysis group.
To represent the geometry of the model, *thin shells* are generally used. These elements are basic geometric shapes (rectangles, cylinder, disks, ellipsoids, etc), defined by points in a three dimensional reference system. With a combination of all these surfaces, the GMM can be created. At least one node is associated to each surface but it can also be divided on more than one node along u, v directions. These direction assume different meanings on the different shapes, for example on rectangles they are the x, y, for cylinders they are z, θ, for disks they are r, θ and for ellipsoids they are θ, ϕ. The nodes numeration can be done automatically (giving an initial ID, it is incremented by one for each node of the surface) or manually to each node. To every surface a thickness can be attributed which is used to compute the mass of the shell and its thermal capacity.
The nodes in which a surface is divided are used to concentrate all the physical properties of the portion of surface they belong to. There are three types of nodes:

- Diffusion nodes have finite capacitance thus they can store and release energy by increasing/decreasing temperature. When the conditions around the node change, there is a transitory before a new equilibrium is reached.
- Arithmetic nodes have zero capacitance thus they react instantly to a change in their boundary condition reaching a new equilibrium.
- Boundary nodes have infinite capacitance thus their temperature is not influenced by their surroundings. This means that the temperature of a boundary node is constant or it can be time varying if the user defines an array.

Note that every node must be connected to the thermal network to be able to run the analysis: if a even a single node results to have no connection the analysis will fail.
In the nodal network, nodes are connected to each other by conductances. They can be of two kind (considering only conduction and radiation): radiative (Radks) and conductive. Radks are computed within the radiative analysis while conductive connections are computed automatically for node that belong to the same shell. For nodes on different surfaces it is necessary to use the *conductor* command to define a connection between nodes. On

TD there are different types of conductors but in this analysis only the Node-to-Node generic conductor will be used. This conductor can be *one way* (the heat is allowed to travel only from one node to another and not vice versa) or *bidirectional* (symmetric connection); the latter will be used. The generic conductor can be defined as a constant value (measured in W/K) or it can be time or temperature dependent. The value of the conductor is computed "manually" by the analyst from geometric considerations and then inserted in the solution process.
Thermal Desktop also allows the analyst to model many thermal components with ad-hoc commands. Those used in this analysis are:

- Heat loads: can be applied to a surface or a node and can be defined in many different ways as a flux or a total load, as constant or temperature/time dependent. This command is useful to model the thermal dissipation of electronic components.
- Thermo-electric coolers (TECs): this command can model only single stage coolers, for multistage they have to be stacked. It requires the definition of two surfaces (in the same submodel and with identical nodalization), one for the hot and one for the cold side. Some parameters of the TEC are necessary for proper simulation and it can be controlled via current/voltage/power.

The last fundamental addition to the model are the boundary and initial conditions. These can either be applied with specific commands to obtain very detailed definition or can be simulated by the analyst with the creation of appropriate shells and symbols. Given the still relatively high uncertainty of the conditions, they have been imposed manually exploiting boundary shells and symbols to obtain a parametrization that is more easily controllable.
After all these steps have been completed, the TMM of the component can be considered ready for analysis.

3.1.3. Heating environment definition

The heating environments are used to compute the environmental heat fluxes due to direct and reflected solar radiation and to infrared heating from other external sources. In TD a heating environment is created by defining an orbit on which the satellite will be placed. It is possible to define different kinds of orbits but for this study case only two definitions have been used. A Keplerian orbit can be defined by inputting Keplerian parameters that characterise the shape, inclination an orientation of the orbit; this has been used to perform preliminary tests on the model. A Latitude, Longitude and height definition has been exploited to represent the operational orbit of LUMIO since it is a halo orbit that

cannot be represented by Keplerian parameters. Note that in this definition the planet is considered as a perfect sphere and the reference system for latitude and longitude is geocentric.
After defining the orbit, it is possible to specify additional constraints for the satellite and for the environment:

- Orientation: specify where the z axis of the model is pointing (nadir, Sun, star, velocity vector), there is also the possibility to define a secondary pointing requirement on either x or y axis which is subordinate to the z pointing.
- Position: define the locations along the orbit where computations will be performed.
- Planetary data: specify the planetary constants of the central body (the data of the main Solar system planets are stored in TD). It is also possible to define the albedo of the planet as constant or latitude and longitude dependent.
- Solar data: specify the Solar flux as a constant or as a time dependent value.

3.1.4. Model checks

Before executing the analysis it is important to verify that there are no macroscopic errors in the model, to do so TD gives the analyst different checks to perform to ensure the model is formally correct:

- Display active sides: with this command the surfaces are highlighted in a specific color code to show active/inactive sides in the current radiation analysis group.
- List duplicate nodes: if there are nodes with the same ID in the same submodel, they will be reported to be corrected if necessary.
- Calculate mass: this command computes the mass of the selected portion of the model (or of the entire model). This check is very simple but useful to verify that the simulation will return adequate transitory response.
- Plot orbit and vehicle: it is also possible to have a visual representation of the environment defined, The model can also be represented in the position of the orbit defined as computation points.

3.1.5. Solution process definition

TD allows the definition of multiple analysis cases (case sets) with the use of the *case set manager* command. Each case set is independent from the others and unique settings can

be given to each of them.
The first step when creating a case set is to define which calculations are going to be performed and the type of solution. The possible calculations include radiation calculation, conductance/capacitance file creation, generation of input model, running and post processing of the analysis. To perform a complete analysis every option must be activated but it is also possible to run partial analysis (only conduction/radiation). The solution types of the analysis can be specified to be steady state, transitory (with additional steady state before/after/both the transitory), cyclic or parametric (in parametric analysis a symbol must be defined to be swept from an initial value to a final value with a certain increment). The convergence criteria of the analysis case can also be defined as maximum number of iterations, maximum ΔT or as system/nodal level energy balance.
Focusing on the radiation tasks, it is possible to select which radiation analysis groups to analyze and which operations to be performed on each of them. The radiation operations include the evaluation of radiation conductors between surfaces, the computation of environmental heating rates (it must be specified which orbit to use) and more. The calculation method can also be specified as Monte-Carlo ray tracing or progressive radiosity method, for the analyses presented in this thesis only Monte-Carlo ray tracing has been used.
For each case set the desired outputs can be specified to be saved as text file and/or for color post processing inside the software.
Finally, for each case set, the necessary overrides can be defined. These can regard initial conditions (can be specified to be certain conditions deriving from previous analyses), properties databases or symbol values.
Some more advanced settings are also available but they will not be covered here since they have not been exploited.

3.1.6. Run and post-processing

When the case sets have been completed, the analysis can be launched. Once it has been completed, the text outputs will be saved in the directory and graphical results can be visualized.

4 | LUMIO-Cam model and analyses

In this chapter the creation of the LUMIO-cam GMM and TMM models will be described. The initial objective of the thesis was to perform thermal analysis of the entire phase-B model. Due to criticalities in other subsystems (that are now being solved) however, the project was subject to some delays. As a result the new complete model is still not available. The objective of the thesis has then be redirected to performing phase-A design review of the payload aiming at consolidating some aspects. The analyses comprehend detector survivability (imposed by system requirement PLD.060, [14]), a simple study of two non-operative worst case configurations and a preliminary analysis of operative conditions. Survivability analyses are necessary because during the entire lifetime of the satellite there is the possibility that the Sun enters directly in the FoV of the optical instrument; studying this situation is necessary to ensure that the detectors do not get damaged. The survivability analysis is in fact the base to assert whether if a mechanical shutter may be necessary. The study of non-operative case aim at determining if the system satisfies basic requirements in the worst non-operative conditions to ensure that the thermo-mechanical design is adequate and, if there are possibilities to improve it. Finally, the preliminary operative analysis has only the objective of assessing the capability of the system of stabilizing the detectors at -20°C when performing observations. These analyses are also useful to determine thermal interface requirements between the payload and the platform.
The CAD model used to perform these studies is the final output of phase-A design of the optical payload. The results obtained from these calculations will however be very helpful to proceed with the final design even if the model is slightly different.

4.1. Modelling

In this section the modelling steps previously described will be applied to the specific case and briefly commented to highlight particular decisions.

4.1.1. Properties databases

All the values in this model have been assumed to be independent from temperature, pressure and wavelength. The only material(s) subject to environmental degradation are the radiator and the lenses coatings. To account for BOL and EOL conditions, given the low number of properties to change, the symbol method has been used. The symbol *BE* has been defined with a nominal value of 2, this value is changed in every case set to 0 or 1 to indicate respectively BOL or EOL conditions.
The numerical values of physical and optical properties used in this model are reported in Tab.(4.1) and Tab.(4.2).

Name	k $[w/m^2K]$	ρ $[W/m^3]$	c_p $[J/kgK]$
Al	121.2	2770	921.6
Cu	385	8960	385
EB	14	3500	1020
FS	0.72	2203	772
Glasses	1.11	3530	389
Kyocera	150	3400	710
TEC	2.11	7740	165
Ti	7.8	4430	522

Table 4.1: Thermo-physical properties database

Name	α	ε	τ_{VIS}	τ_{NIR}
Al	0.16	0.03	-	-
Black coating	0.9	0.9	-	-
Cu	0.3	0.03	-	-
EB	0.8	0.8	-	-
FS	0.9	0.75	-	-
Glasses BOL	0.066	0.785	0.896	-
Glasses EOL	0.102	0.786	0.86	-
Kyocera	0.9	0.9	-	-
Ti	0.4	0.55	-	-
White paint	0.2	0.9	-	-

Table 4.2: Thermo-optical properties database

4.1.2. Model creation

Starting from the phase-A CAD model of the LUMIO-cam, the overall system has been divided in eight submodels, to each has been assigned a certain interval for the nodes IDs:

BOX (1000-7000), *OPT_CH* (8000-15999), *BAFF* (16000-18999), *SUPP* (19000-29000), *CCD1* (30000-36000), *CCD2* (40000-46000), *LENS* (50000-50005), *RAD* (60000-60001). Images of the submodels are reported in Fig.(4.5).
With regard to radiation analysis groups, two of them have been defined: *EXT* group comprehends all surfaces that interact with the outer environment (deep space or the interiors of the satellite's structure), *INT* group on the other hand is the collection of all surface inside the camera's structure.
To generate the GMM of the LUMIO-cam, the thin shell geometric shapes used are: rectangles, disks, cylinders, ellipsoids and polygons. The most difficult geometries to represent were:

- Pierced rectangular shells such as those where the optical barrel enters the main box. This kind of geometry is problematic because Thermal Desktop does not have the possibility of performing Boolean operations between shells. To get around this problem, the adopted solution is that of splitting the rectangular surface in an irregular shape represented with polygons.
- Surfaces with big thickness variations. The most challenging subsystem to represent is the *SUPP*, here the geometry is very complex and the walls have many flarings and cuts to lower the mass of the component. In this case the adopted solution has been to use a higher number of shells to define different thicknesses.
- Surfaces partially in contact and partially free. When this situation was present, the logic was to consider the entire surface active/inactive for radiation if one of the two conditions was predominant (free surface larger than contact surface and vice versa). When this approximation was not possible, the single surface was separated and modelled as two distinct nodes with different activity.

For the high majority of surfaces a sufficient level of detail is to associate them to a single diffusion node. A more detailed nodal subdivision is used for the baffle and optical channel: three nodes are used in the angular direction to capture possible temperature gradients. These gradients could be present as a result of the camera's position inside the main structure: being placed next to two external surfaces and having many adjacent components dissipating power, the boundary conditions may lead to a complex temperature distribution. The optical barrel is subject to an even higher level nodal division: since this component has the crucial role of holding the lenses in place it is fundamental to know the temperature gradients responsible of thermo-elastic deformation that could cause an undesired variation in the focal length. For this reason, along the axial direction particular attention was given to ensure that a series of nodes is placed in correspondence

of every lens.
All the nodes have been connected with the appropriate radiative and conductive conductors. The radiation calculations were performed automatically by the software during the solution of each analysis case and the same was done for the conduction between nodes belonging to the same surface. To conductively connect different surfaces the computations were performed manually exploiting the thermal resistance concept of every involved geometry, parameterising the computations from a geometric and thermo-physical properties point of view.
The components that dissipate power inside the LUMIO-cam are only the detectors and the TECs. The detectors dissipation can be modelled with heat loads on the corresponding surfaces while TECs' dissipation is managed autonomously by the software when they are modeled with the specific command. Considering the non-operative cases, the detectors and electronic boards will not dissipate any electric power so as the thermo-electric coolers unless the are switched on, if necessary. In the survivability analyses the only thermal load present is the environmental flux entering from the aperture and being focalised on the detectors. This has been introduced in the model as a total load on the shells corresponding to the detectors, the calculations performed to compute the value of these loads will be presented in the next section. In the cold non-operative cases no heat loads are present while in the operative cases electric power dissipation has been applied to the detectors together with the environmental fluxes due to Moon's surface observation.
To represent the boundary conditions an additional submodel was introduced (BC_BOX) in which external walls were created, to simulate the structure of the cubesat. This representation was necessary to prevent direct interaction of the entire LUMIO-cam with deep space and to set some fixed boundary temperatures (the boundary temperatures were parameterised and taken from an environmental analysis of the satellite's structure performed by the platform provider). The radiator of the LUMIO-Cam is in this subsystem, placed on the panel in the $+y$ direction and covering 25% of its surface.
The initial conditions on temperature of every surface of the LUMIO-cam were imposed equal and parameterised with a TD symbol T_0 which is then set to the desired value for each analysis case.

4.1.3. Heating environments

To perform all the analyses, three environments have been defined: one for the survivability analyses, one for the non-operational and finally one for the operative cases. Since all these analyses are preliminary, it was sufficient to consider simplified orbits. This was possible also thanks to the fact that the boundary conditions imposed for each case were

computed on the real case orbit.
For the survivability and non-operational analyses, the same orbit has been used with different satellite orientation. The orbit is Moon centered, polar and circular with a radius of 60000 km and a β angle of 90° (the angle between solar vector and the plane of the orbit), it has been defined in TD using the dedicated orbit management tool. In the survivability case the satellite is oriented with the LUMIO-Cam pointing towards the Sun while in non-operative cases the optical instrument looks at deep space. The two orbits previously described are represented in Fig.(4.1).
For operational analyses the orbit is again Moon centered and circular with a radius of 60000 km but it is now an equatorial orbit. The satellite is oriented with the optical axis ($+z$ axis of the model) always pointing towards Moon's surface and the $+x$ axis aligned with the velocity vector, this configuration ensures that the radiator panel (positioned in the $+y$ direction) is constantly pointed to deep space.

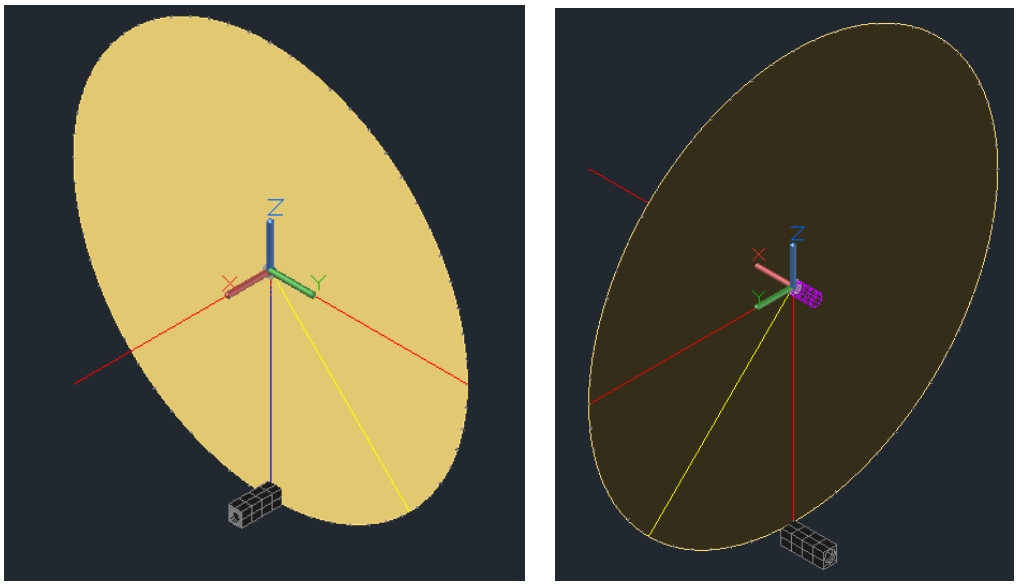

(a) *Sun pointing orbit* (b) *Space pointing orbit*

Figure 4.1: Radiation environments

4.1.4. Model checks

The active side display check has been performed to ensure that every surface was set in the appropriate radiation analysis group with the correct activity level (see Fig.(4.2)). The mass of every submodel and of the entire model has been computed to compare them with the phase-A mass budgets (see Tab.(4.3)).

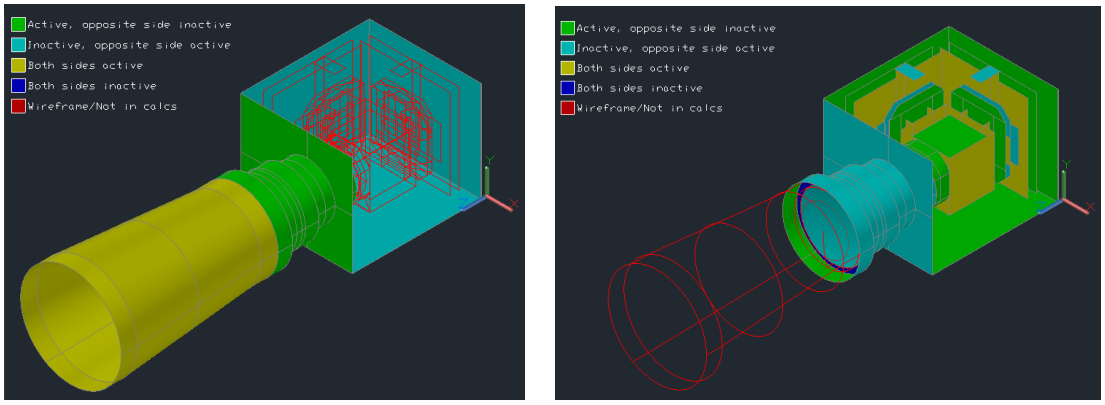

(a) *EXT group* (b) *INT group*

Figure 4.2: Radiation analysis groups active sides display

Name	Mass $[kg]$
BAFF	0.20593
CCD1	0.15225
CCD2	0.15232
BOX	0.80639
LENS	0.42941
OPTCH	0.20679
RAD	0.14542
SUP	0.18064
TOTAL	2.279166

Table 4.3: Subsystems mass

4.2. Analysis case set up

Seven analysis cases have been defined: the first three are dedicated to survivability analyses, Case 4 and 5 are the non-operative ones wile the last two cases are the operative conditions. Some common parameters can be defined for all cases such as the computations to be performed (must comprehend both radiation and conduction analysis), the radiation tasks (compute radiation conductances for *EXT* and *INT* groups and environmental fluxes only for *EXT*) and the radiation parameters (in the Monte-Carlo analysis use of 5000 rays per node with an energy cutoff factor of 0.1). The outputs necessary to perform post processing are: the temperature, the heat flux and the capacitance associated to each node. All these data have been saved both in the form of output files and graphical post-processing data.

The symbols defined in the model are: *BE* to specify BOL (BE = 1) or EOL (BE = 2)

conditions, *Q_ NIR* and *Q_ VIS* to specify the heat loads on respectively the two detectors, *T_ 0* to specify the initial temperature of the model, *Teccontrol* to switch on/off the TECs (1 = ON, 0 = OFF). Also the boundary temperatures have been defined using symbols.

	BE	T_0 [K]	Teccontrol	Q_VIS [W]	Q_NIR [W]
Case 1	2	253.15	0	1.012	0.178
Case 2	2	273.15	0	1.012	0.178
Case 3	2	273.15	1	1.012	0.178
Case 4	2	273.15	0	0	0
Case 5	1	273.15	0	0	0
Case 6	2	253.15	1	1	1
Case 7	2	253.15	0	1	1

Table 4.4: Survivability analyses symbols

Detector survivability analyses

The questions at the base of the survivability analysis are:

- Does the presence of the Sun in the FoV compromise the detector's survivability?
- Is the temperature increase coherent with detector's limits?
- What temperature is reached after introducing the Sun in the FoV?

The conditions in which survivability analysis has to be performed have been identified by studying the attitude of the satellite in its entire lifetime. Two critical cases have been identified: the first is during attitude maneuvers when the Sun is visible for around four minutes and the second during propulsion maneuvers when the Sun stays in the FoV for around twenty minutes. Taking into consideration the worst case (highest exposure time), three main cases will be set-up for analysis with different TEC activity and initial conditions (the end time of every analysis is 1200 seconds corresponding to twenty minutes of exposition):

1. TEC off, $T_0 = -20°C$
2. TEC off, $T_0 = 0°C$
3. TEC on, $T_0 = 0°C$

All these three cases have been defined separately in TD using the case set manager. The override option is used to set the symbols to the appropriate value for each analysis, the

values of each symbol for Cases 1-3 are reported in Tab.(4.4).
It is important to underline is that TD computes environmental loads only on surfaces that are directly interacting with the environment (in this case only the EXT analysis group is considered). For this reason, and because it is not possible to define the absorptivity as wavelength dependent (this aspect is important because the lenses have different filtering effect in the two channels), to simulate the environmental load reaching the detectors the computations have been performed manually.
The two wavelength bands of interest are: 450-800 nm (VIS) and 850-950 nm (NIR). Approximating the Sun as a blackbody with a temperature of 5800 K and a total emitted flux of 1353 W/m^2 at an average distance of 1 AU, it is possible to retrieve from tabulated data (available in [16]) the fraction of the total emission in each band ($F_{\lambda_1 \to \lambda_2}$) and compute the power in that band ($E_{\lambda_1 \to \lambda_2} = E_{tot} F_{\lambda_1 \to \lambda_2}$):

Band	$F_{\lambda_1 \to \lambda_2}$	$E_{\lambda_1 \to \lambda_2}$ $[W/m^2]$
VIS	0.39957695	540.6276134
NIR	0.0671561	90.8622033

Table 4.5: Band emission values

Tab.(4.5) reports the power flux emitted by the Sun in the two interest bands. Considering the capture area of the first lens (0.00283 m^2), the actual power entering the system and reaching the detectors is: 1,012 W in the VIS channel and 0,178 W in the NIR. These values have been obtained by multiplying the fluxes reported in Tab.(4.5) by the aperture area and accounting for the fraction of power absorbed by the lenses (different absorption in the two channels) and other components which factors are reported in Tab.(4.6).

τ_{Filter}	$\tau_{Dichroic}$	τ_{Det}	τ_{VIS}	τ_{NIR}
0.95	0.9	0.9	0.86	0.9

Table 4.6: Transparency factors

The boundary conditions are the same for every survivability case and are reported in Fig.(4.3) and Fig.(4.4).

Non-operative worst cases

Cases 4 and 5 analyse a timespan of 40000 s to allow the system to reach an equilibrium conditions. The symbol values are reported in Tab.(4.4). The boundary conditions of Case 4 (which is the non-operative hot case) are again the same of the survivability cases

while for Case 5 (non-operative cold case with the LUMIO-Cam looking at deep space) the conditions are reported in Fig.(4.3) and Fig.(4.4).

Operative cases

Given the objective of the preliminary operative analysis (determine of the system is able to keep the detectors at -20°C during operations), only the hot case has been considered. The configuration is reported in Fig.(4.3) and the boundary condition thermal map in Fig.(4.4).
Initial results of analyses performed on the phase-A design showed that the design was unable of satisfying the temperature requirement on the detectors. This conclusion led to the necessity of performing minor changes in the design to improve/reduce heat flows between components. The modification process (made simple by the model's parametrization) was iterative and led to the following changes in the design:

- The thermal straps have been assumed to have an overall conductance of 0,5 W/K (higher than the value computed from CAD geometry). This change allowed to discharge heat more effectively from the TEC's hot side to the radiator and to standardize the payload-structure thermal connection used by this model to that used by the platform provider.
- The support previously present to mount the TECs to the thermal straps has been removed. This modification reduced the heat back-flow from the TECs' hot side to the detector. Removing the supports means that each TEC will have to be attached to the corresponding thermal straps by brazing the two components.
- The connection between the electronic board attached to the detector and that attached to the LUMIO-Cam's structure had to be reduced due to the excessive heat coming from the structure and reaching the detectors.
- The radiator size was increased up to 100% of the $+y$ panel surface (Fig.(4.5)). Increasing the radiator's surface allows a higher dissipation to deep space. This change does not affect compatibility with the structure as the platform provider was already considering a radiator of similar dimension. The radiator was connected to the boundary surfaces with eight titanium washers each with a conductivity of 0,02 W/K.

The heat loads applied to the detectors are respectively 0.8 W and 0.72 W for the VIS and NIR channels. These values were computed assuming a 10% electrical power dissipation and the environmental flux due to Lunar albedo. The albedo contribution has been

estimated by multiplying the values found for the survivability analyses by a mean Lunar albedo factor of 0.14 (taken from [10]). This is equivalent to performing observation when the Moon is fully illuminated by the Sun which is clearly an overestimation. The real operative conditions in fact foresee scientific observation with a maximum lunar surface illumination of 50%.

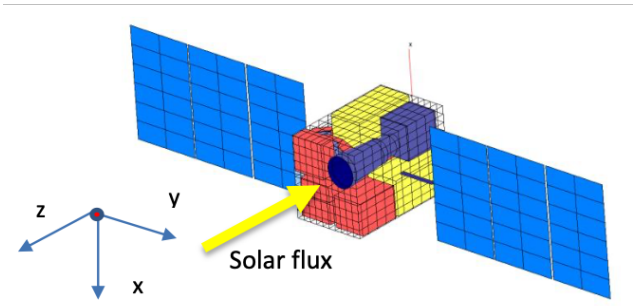

(a) *Survivability*

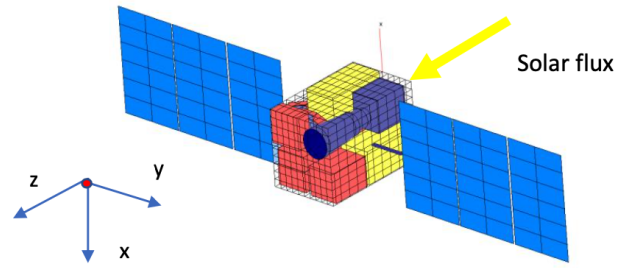

(b) *Cold non-operative case*

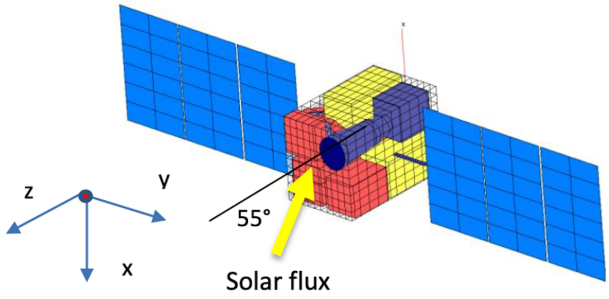

(c) *Operative case*

Figure 4.3: Boundary condition configurations

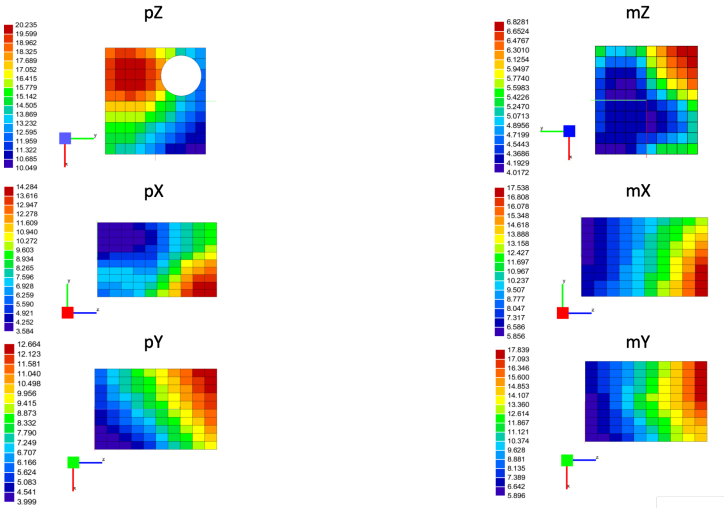

(a) *Survivability cases*

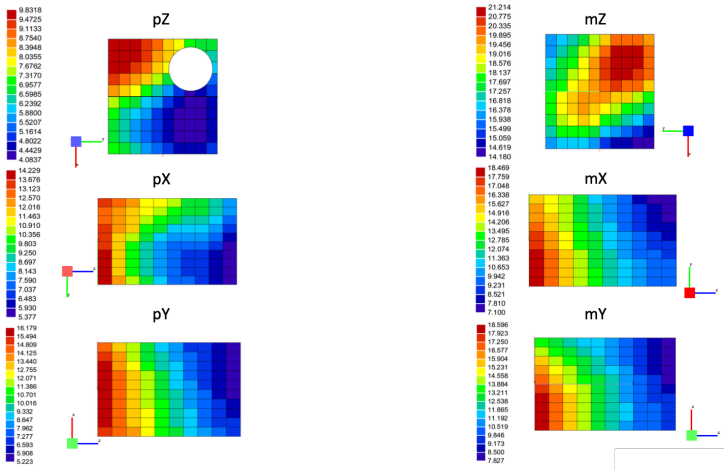

(b) *Cold non-operative case*

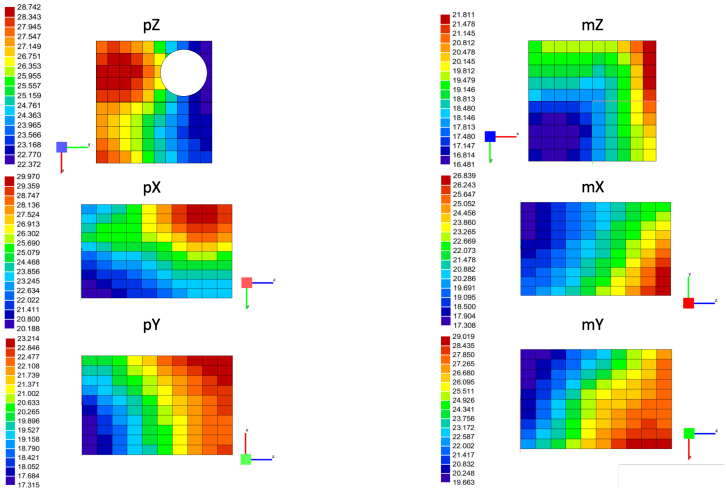

(c) *Operative cases*

Figure 4.4: Boundary conditions thermal maps

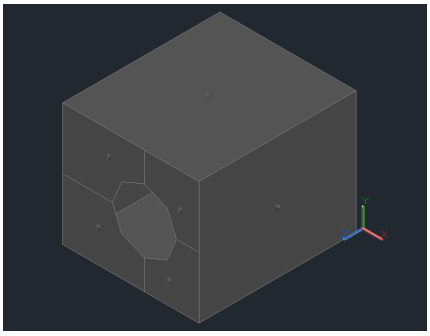

(a) *BOX subsystem*

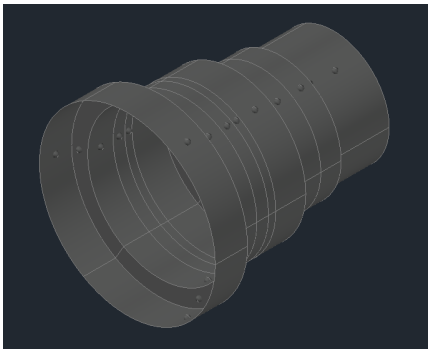

(b) *OPT_CH subsystem*

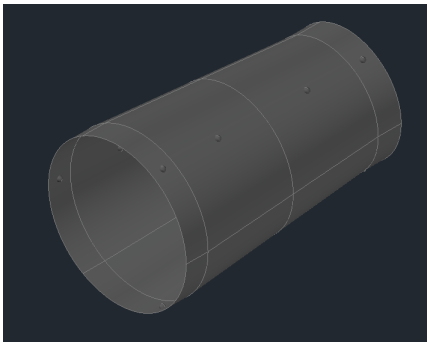

(c) *BAFF subsystem*

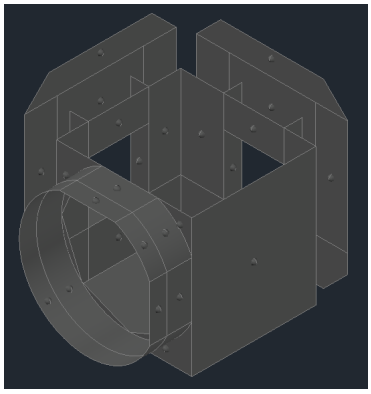

(d) *SUPP subsystem*

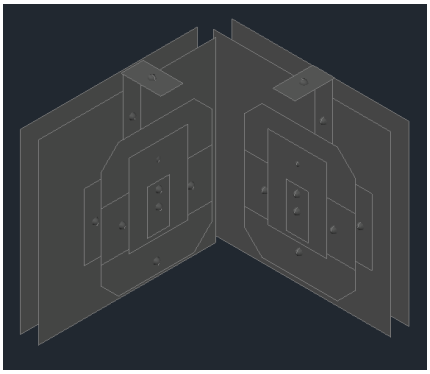

(e) *CCD1 & 2 subsystems*

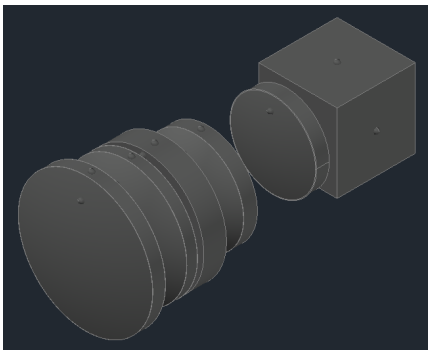

(f) *LENS subsystem*

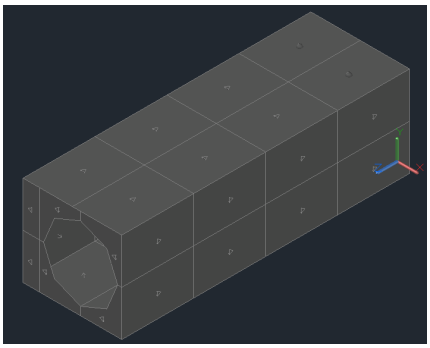

(g) *BC_BOX subsystem*

Figure 4.5: Model subsystems

5 | Results and post processing

In this chapter the results of all analysis cases will be reported and commented according to the objective.
To have a benchmark to comment the results obtained, the detector's datasheet [15] and the system requirements document [14] have been consulted to establish some limits. From the detector's datasheet the limits reported in Tab.(5.1) have been determined while from the SRD of phase B the requirement PLD.210 and PLD.220 impose respectively a survival temperature range of -30°C +50°C (TBC) and an operative range of -20°C +40°C (TBC).

Description	Min	Max
Operational range	-120°C	+75°C
Non-operational range	-200°C	+100°C
Rate of change		5°C/min

Table 5.1: Detector thermal requirements

5.1. Survivability analyses

The limits determined were considered to answer the questions of section 4.2.

5.1.1. Cases results

Case 1

The results in Fig.(5.1) show that the final temperature of the detector in the VIS channel is of around -14.81°C while for the NIR channel it is of -19.13°C. The higher temperature in the first waveband is consistent with the higher flux to which it is subject. Considering the VIS channel (which is subject to the greatest ΔT), the averaged rate of change of the temperature is of 0.26°C/min while the maximum rate of change is in the first four minutes and has a value of $\simeq$0.90°C/min. The overall highest temperature is reached by the tip of the baffle (-1.77°C). With these results it is possible to state that the survivability

requirements of the detectors are satisfied in this case.
Fig.(5.2) shows the temperature mapping after 20 minutes of exposition, the images have been generated using TD's graphical post processing tool.

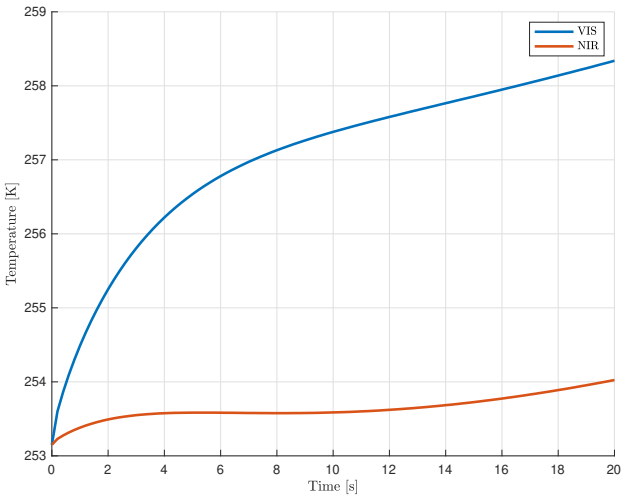

Figure 5.1: Detector temperatures, Case 1

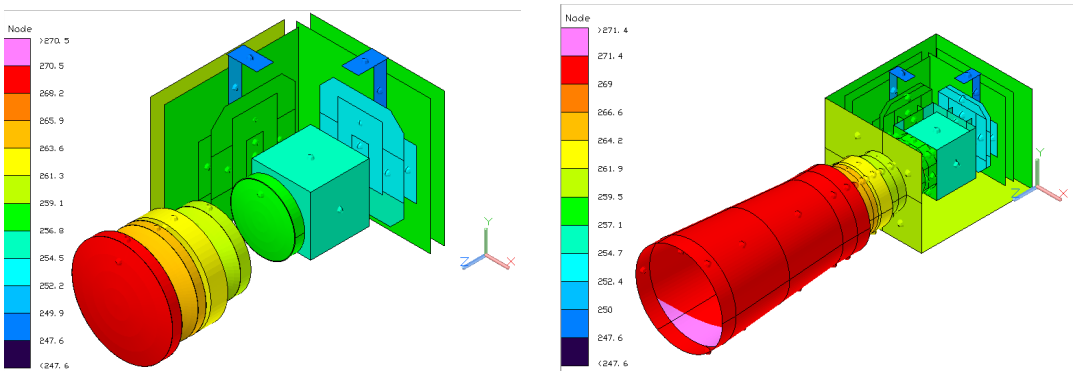

(a) (b)

Figure 5.2: Final temperature distribution, Case 1

Case 2

Similarly to the previous case, results for the VIS and NIR channels are reported in Fig.(5.3). The initial temperature increase followed by its reduction can be explained considering the hypothesis of the analysis: the temperature of every component is imposed equal at the beginning thus the heat flux applied to the detectors causes their temperature to increase in the first instants of analysis. Once the components start interacting with each other, the heat is conducted from the detectors to the radiator, where it is dissipated,

though the thermal straps and this causes the reduction. The time scale in which this happens is different in the two detectors due to their different heat fluxes. The final temperatures reached by the detectors are of around 2.47°C and -1.79°C for the VIS and NIR channels respectively. Again, the two different temperature are caused by the different heat loads. The highest rate of change of the temperature is recorded in the visible band in the first six minutes with a value of 0.52°C/min. The maximum overall temperature of 8.85°C is again reached in the baffle.
The temperatures reached in this case and the rate of change are well inside the acceptable ranges thus survivability requirements of the detectors are satisfied also in Case 2.
A temperature map of Case 2 is shown in Fig.(5.4).

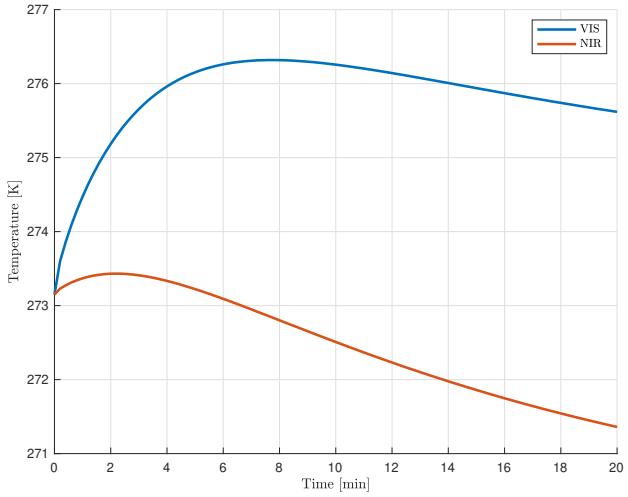

Figure 5.3: Detector temperatures, Case 2

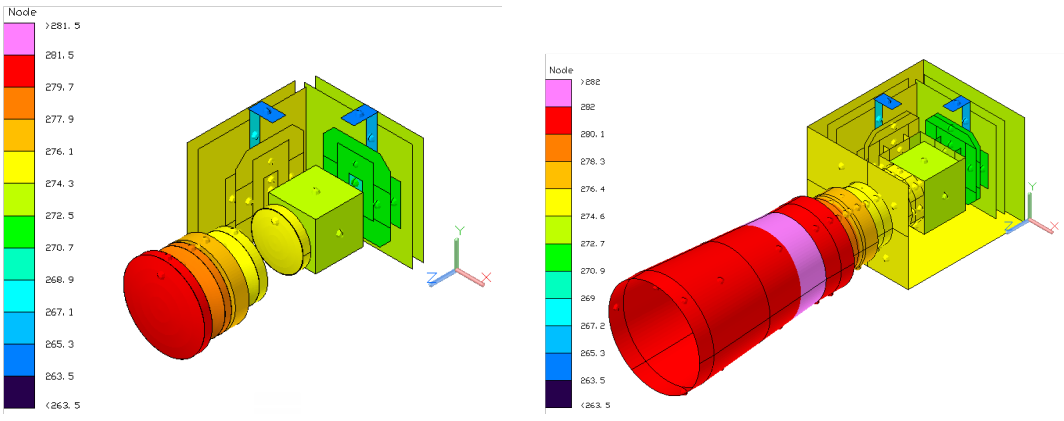

(a) (b)

Figure 5.4: Final temperature distribution, Case 2

Case 3

The detectors temperature evolution of Case 3 is reported in Fig.(5.5) the final temperatures are 1.99°C (VIS channel) and -2.04°C (NIR channel). The maximum rate of change in the temperature is ≃0.45°C/min in the VIS channel. The highest temperature in the system is once again reached in the baffle with the same value as Case 2 (8.85°C). Survivability requirements of the detectors are satisfied also in Case 3.
Fig.(5.6) reports the final temperature map of Case 3.

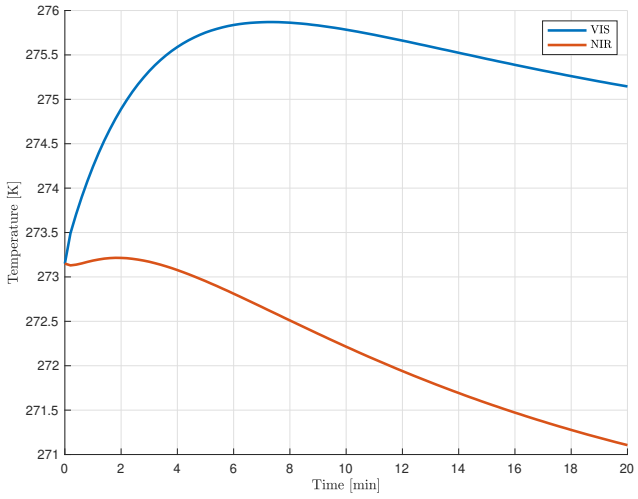

Figure 5.5: Detector temperatures, Case 3

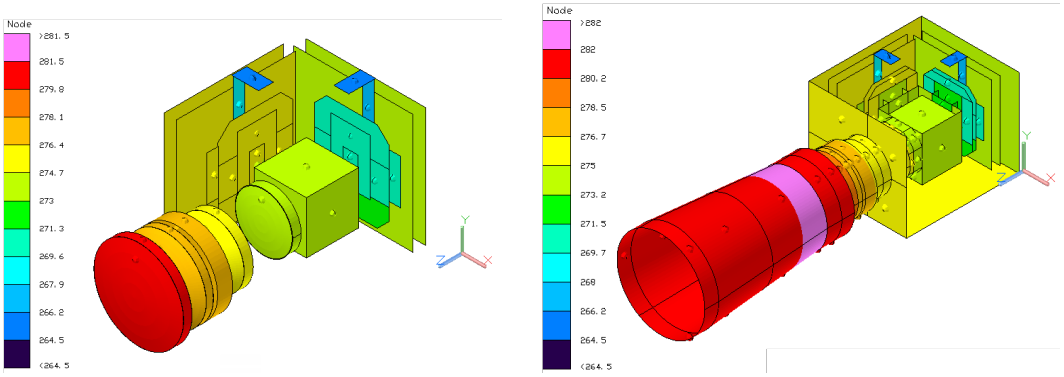

(a) (b)

Figure 5.6: Final temperature distribution, Case 3

5.1.2. Comments

By observing the results of the three survivability analyses the ability of the detectors to survive direct Sun exposure can be assessed (thus verifying the PLD.060 requirement). The need of a mechanical shutter can be completely discarded avoiding the additional mass and complexity and maintaining the highest possible system reliability.
A comparison of the detectors' temperature in cases 2 and 3 is reported in Fig.(5.7). It is evident that in Case 3 the detectors are maintained at a slightly lower temperature. This is possible because the TECs are actively pumping heat away from the detectors to the thermal straps. The set-up of these components is however not optimized yet which prevents a proper cooling of the sensitive elements. By finely tuning the parameters of the TECs, it will be possible to maximize the COP (coefficient of performance) thus reducing the waste heat produced during the cooling process.

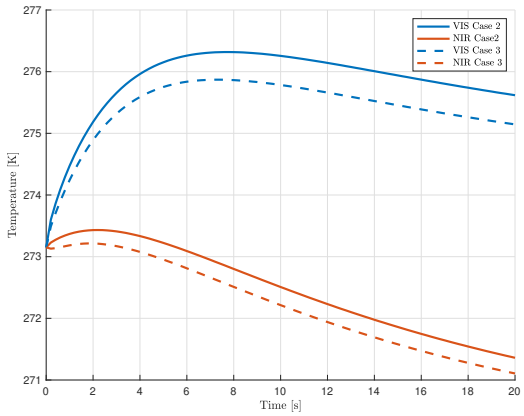

Figure 5.7: Detectors temperature comparison of Case 2 and 3

5.2. Non-operative cases analysis

5.2.1. Cases results

Case 4

As already specified in section 4.2, Case 4 has the same conditions of Case 2 with an extended analysis timespan, allows to study the equilibrium conditions reached after the transient. With the results presented in Fig.(5.8), which shows the temperature evolution of the two detectors, it is possible to confirm that the survivability requirements would be satisfied also for extended direct Sun exposition.

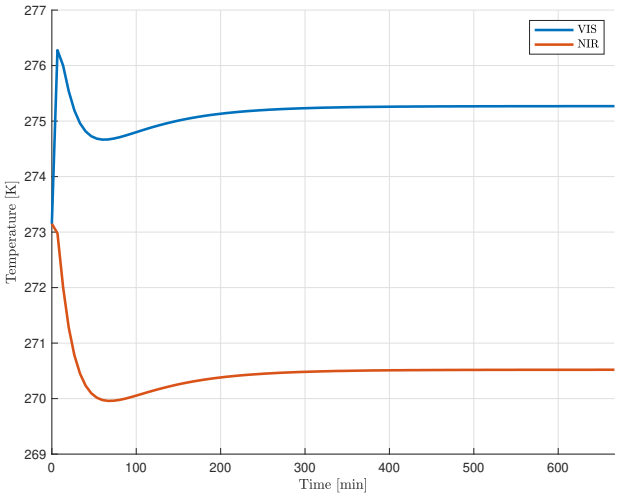

Figure 5.8: Detector temperatures, Case 4

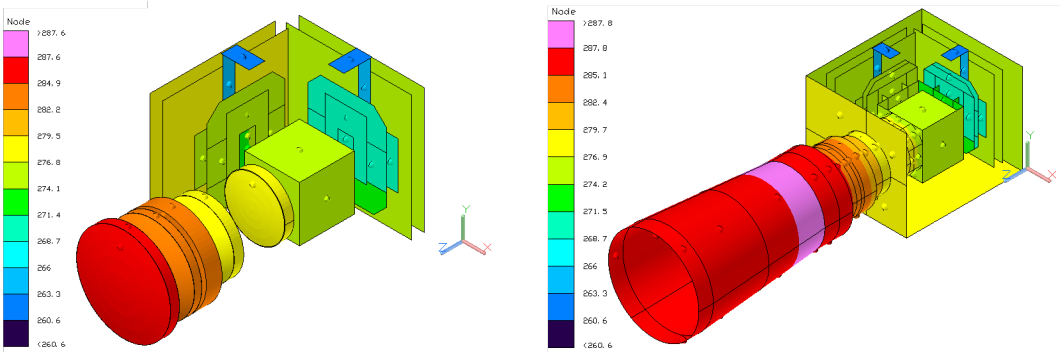

(a) (b)

Figure 5.9: Final temperature distribution, Case 4

Case 5

Fig.(5.10) reports the temperature evolution of the detectors for Case 5. It is evident that the temperature of the two detectors is practically the same and a particular behaviour is noticeable: the temperature initially decreases to a minimum value of -2.99°C (on the VIS detector) to later increase until stabilizing at ≃0.76°C (on both channels). The physical explanation for this trend is that heat from the detectors is rapidly transported to the radiator which dissipates it to outer space. The effect of the boundary conditions (heating the inner components mainly by radiation) requires more time to act because heat leaving the outer surfaces of the structure has to be absorbed and re-radiated by many surface before reaching the detectors.
It is clear again that the temperatures are within the survivability limits.

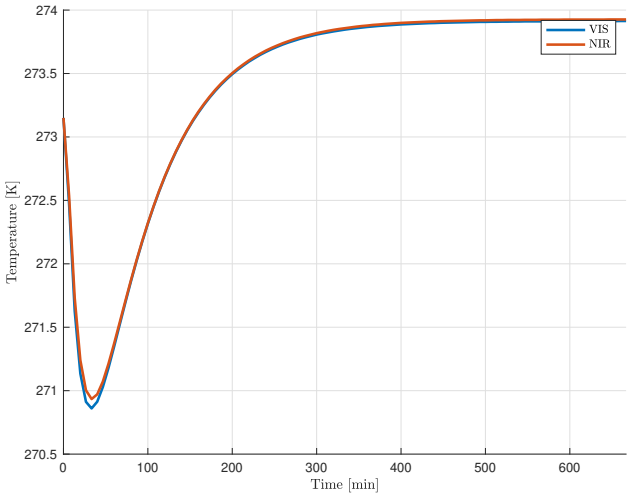

Figure 5.10: Detector temperatures, Case 5

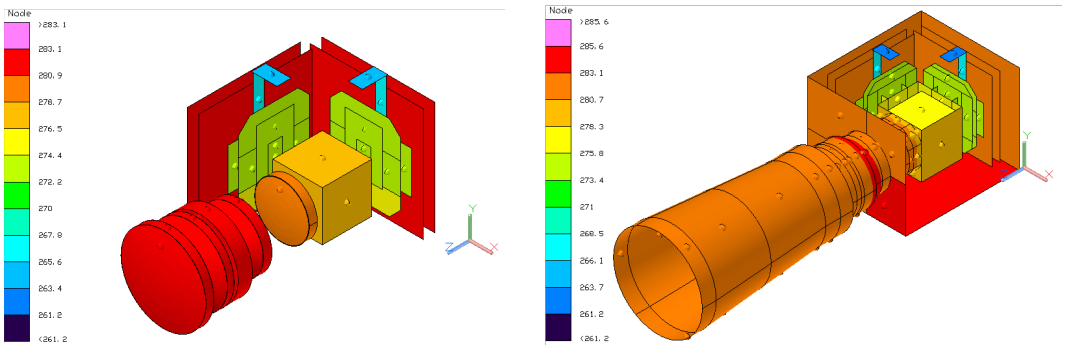

(a) (b)

Figure 5.11: Final temperature distribution, Case 5

5.2.2. Comments

The results of cases 4 and 5 are enough to state that the current thermo-mechanical design satisfy the PLD.210 requirement thus allowing the system to be capable of withstanding both the hot and cold worst non-operative cases without compromising any functionality. Fig.(5.12) reports the temperature of three nodes in the angular direction measured on the optical barrel in correspondence of the first lens for the two worst non-operational cases. It is immediately clear that no appreciable gradient exists in the angular direction, the same is valid for the entire length of the optical barrel and baffle but for simplicity only one axial position has been represented. From the results obtained, a uniform temperature could be expected in many conditions. This conclusion is however limited to the two cases analysed up to now as the temperature distribution strongly depends on the boundary

conditions.

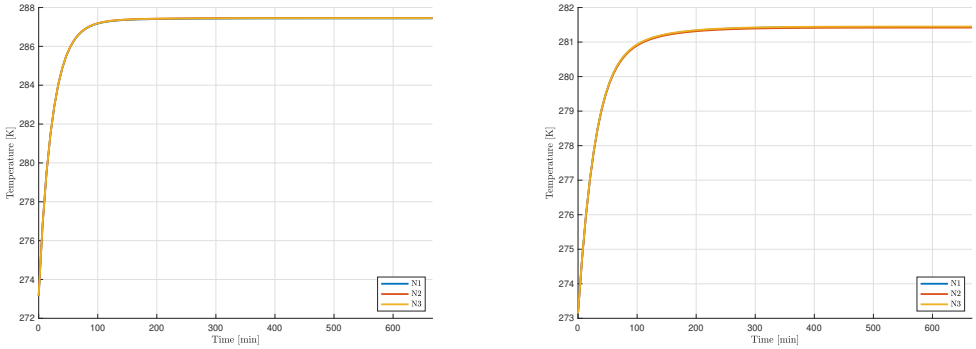

(a) *Case 4* (b) *Case 5*

Figure 5.12: Angular temperature gradients

In Fig.(5.13) is shown the temperatures of a series of nodes (belonging to the optical barrel) in the axial direction. The presence of a gradient along the optical axis is immediately noticeable with a maximum value of $\simeq 9.45$°C in Case 4 and approximately 1.73°C in Case 5. Observing the temperature distribution of Case 5 the conclusion is that inside the optical barrel, the maximum temperature is reached near the middle of the component rather than its tip as in Case 4. This observation is confirmed by looking at the temperature map of Fig.(5.11) generated by the graphical post processing tool of TD.

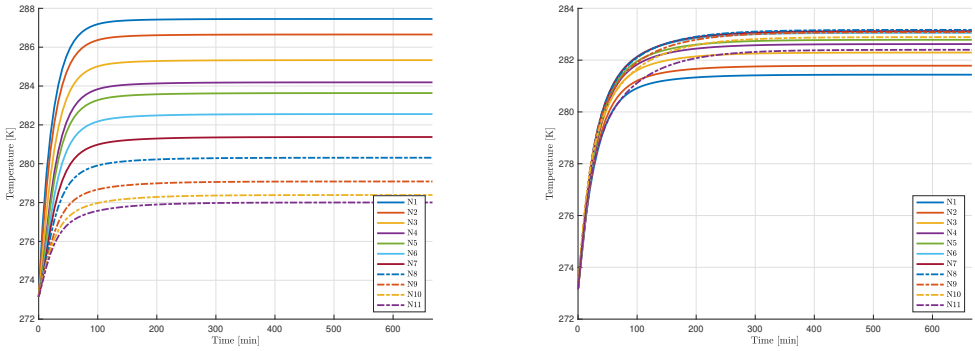

(a) *Case 4* (b) *Case 5*

Figure 5.13: Axial temperature gradients

With the axial temperature distribution available, a detailed thermo-mechanical analysis can be performed to compute the elastic deformations caused by thermal expansion of the material. Particular attention must be given to the nodes in positions corresponding to lens mountings because excessive axial deformations caused by thermal expansion may

lead to a change in the relative positioning of the lenses which would cause the overall optical system to go out of focus. In this context, an important parameter used to measure optical stability is the temperature difference between the first lens and the focal plane assembly. Tab.(5.2) reports the values of this parameter for both channels.

	ΔT_{VIS-L1}	ΔT_{NIR-L1}
Case 4	12.316	17.065
Case 5	7.502	7.490

Table 5.2: Temperature difference between FPA and first lens

Since both Case 4 and 5 are non-operational and no scientific measurements are being performed, the main concern is just to ensure survivability of all the components. Optical stability will be addressed during operative case analyses.
Regarding survivability it is fundamental not only to measure the temperature of the barrel in positions corresponding to lens mountings by also the temperature of the lenses themselves. This is necessary because every material has a different thermal expansion coefficient and an incorrect coupling between the optical barrel, the supports and the lenses could result in high mechanical stresses. These stresses may eventually lead to the optics being damaged thus causing a critical failure of the payload compromising the entire mission. For this reason, it is fundamental to monitor the temperature of each individual lens and keep it inside the acceptable range defined during the design phase. Controlling the temperature of the lenses is particularly difficult because it must be done passively by properly designing the supports and choosing appropriate materials, for this reason thermal analyses performed in the design phase are crucial to verify the validity of the project. Fig.(5.14) reports the temperature of each lens for cases 4 and 5. It is possible to see how in both cases, depending on the position of each lens, the temperature follows the same behaviour of the corresponding nodes of the optical barrel. A brief comment should be done when comparing Case 1 and 4: from Fig.(5.15 a) the lenses appear to have a much lower final temperature than in any other case. This is due to the limited analysis time (20 minutes) and the very low initial temperature of -20°C. It is important to underline again that initial temperature was assumed uniform in the entire model for simplicity but in real cases it is unlikely that lenses reach such low temperatures (as confirmed by the cold case analysis where the minimum temperature in the optics is reached by the dichroic at 4.15°C). Considering a longer period for analysis (Fig.(5.15 b)) the lenses reach a final equilibrium temperature condition identical to that of Case 4 in Fig.(5.14 a). Finally, the maximum and minimum temperature of Case 4 and 5 at equilibrium point are reported in Tab.(5.3). The maximum and minimum temperature are reached respectively at the

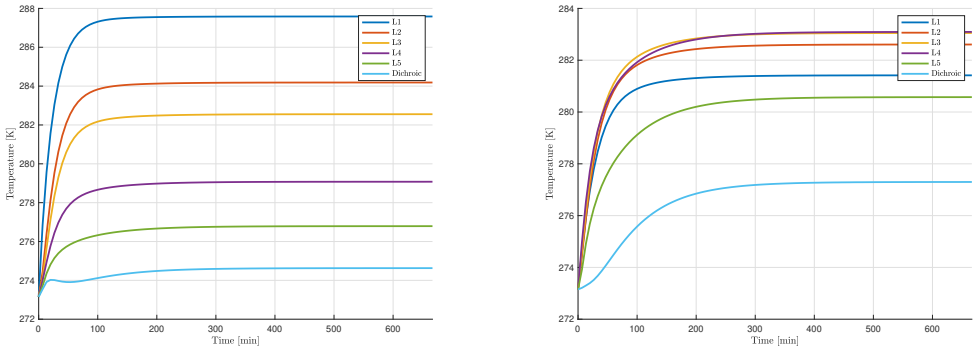

(a) *Case 4* (b) *Case 5*

Figure 5.14: Lens temperature

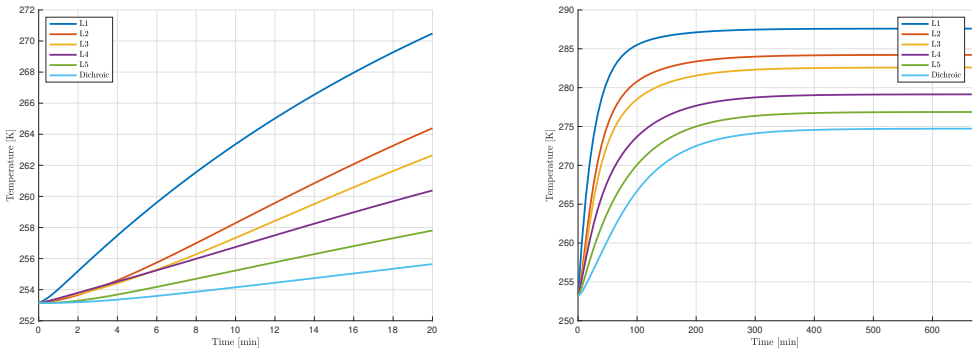

(a) *Case 1 (t=20 min)* (b) *Case 1 (t≃10 h)*

Figure 5.15: Lens temperature Case 1

connection between the baffle and the optical channel and at the interface between the thermal straps and the radiator in Case 4. In Case 5 the minimum temperature is again at the thermal strap-radiator interface while the maxim temperature is reached by the panel in direction -y of the main box of the LUMIO-Cam.

Case	T_{max} [°C]	T_{min} [°C]
Case 4	14.65	-12.55
Case 5	12.45	-11.95

Table 5.3: Max and min temperatures in survival cases

5.3. Operative cases

The analysis of operative cases spans a period of approximately one day of activity.

5.3.1. Cases results

Case 6

Fig.(5.16) reports the temperature trend of the two detectors with the TECs switched on. Neglecting the first part (the behaviour is due to the initial conditions of the system), it is immediately noticed that the detectors are both maintained at the target temperature of -20°C.

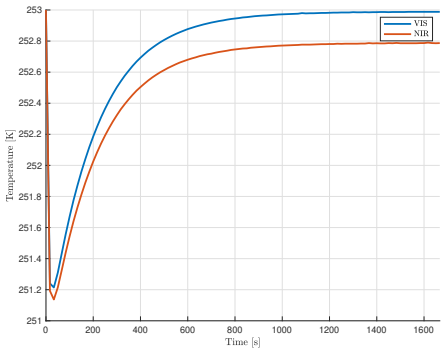

Figure 5.16: Detectors temperature, Case 6

To reach this condition the TECs have to develop a ΔT between the hot and cold side of approximately 4°C (Fig.(5.17) shows the temperature evolution of both sides of the two TECs). It is easy to understand when the TECs are working because the hot side temperature is kept higher than the cold side temperature.

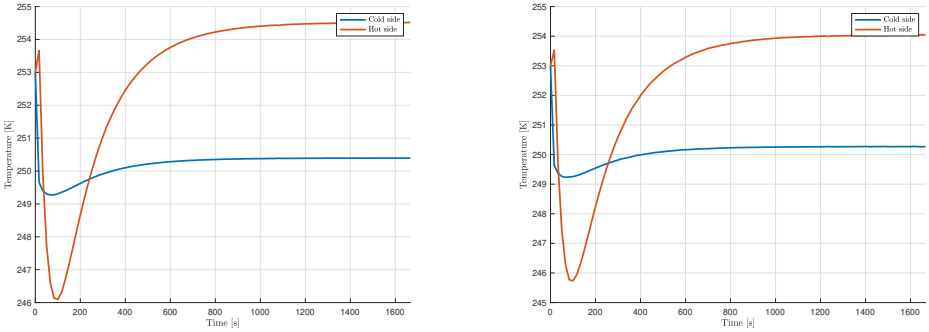

(a) *VIS channel* (b) *NIR channel*

Figure 5.17: TECs temperatures, Case 6

Another important element to be monitored is the radiator. When TECs are switched on, this component receives a heat flux equal to the sum many contributions: the detectors heat loads, the waste heat generated by the activation of the cooling elements, the heat due conductive connection with washers and radiation exchange with other surfaces. The heat is then radiated to outer space to be dissipated. Fig(5.18) reports the average temperature of the radiator panel, the final equilibrium temperature is of approximately -30°C.

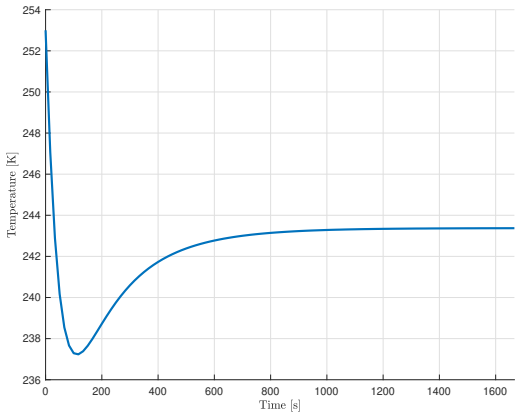

Figure 5.18: Radiator temperature, Case 6

Case 7

The temperature evolution of the detectors when TECs are off is shown in Fig.(5.19). Neglecting again the first part of the graph, the temperatures stabilize at approximately -16.5°C and -17°C (VIS and NIR respectively). These temperatures are close to the target of -20°C but if maximum performances are required, TECs are necessary to ensure that the desired temperature is obtained. Also in this case the radiator temperature is taken into consideration, Fig.(5.20) reports its evolution. Since the TECs are not working, the equilibrium temperature of Case 7 is lower because the contribution due to waste heat is equal to 0 W.

5.3.2. Comments

The results of Case 6 shows that with minor modifications, the system is able of maintaining the desired temperature during operative phases. Case 7 serves mainly to establish interface requirements with the satellite's structure. In fact, if the platform provider is able to guarantee a radiator temperature as close as possible to that of Case 7, it means that the TECs will have to ensure a small ΔT to the detectors thus dissipating a small amount of electrical power.

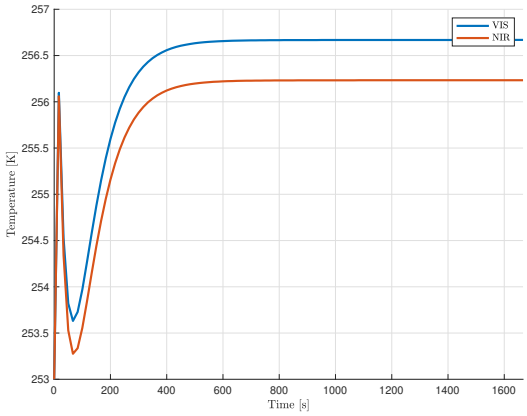

Figure 5.19: Detectors temperature, Case 7

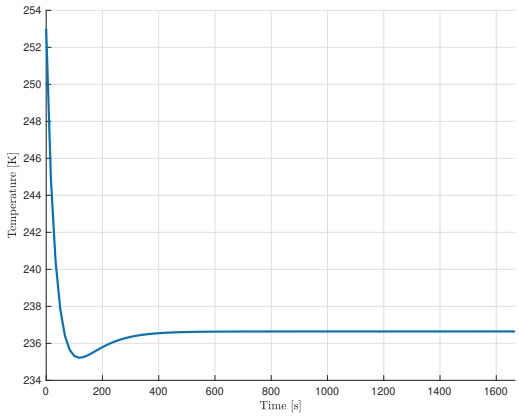

Figure 5.20: Radiator temperature, Case 67

Fig(5.21) reports the temperature evolution of each lens in both operational cases. These results have been used to compute the ΔT_{VIS-L1} and ΔT_{NIR-L1} parameters (reported in Tab.(5.4)) that can be used in the system's optical stability assessment.

	ΔT_{VIS-L1}	ΔT_{NIR-L1}
Case 6	27.964	28.165
Case 7	24.502	24.938

Table 5.4: Temperature difference between FPA and first lens

The values of the temperature difference between the first lens and the two focal plane assemblies are too high when compared to those used in the design process ($\Delta T = 20 \pm 4$). This means that the thermal design of the instrument must be further modified to reduce this temperature difference.

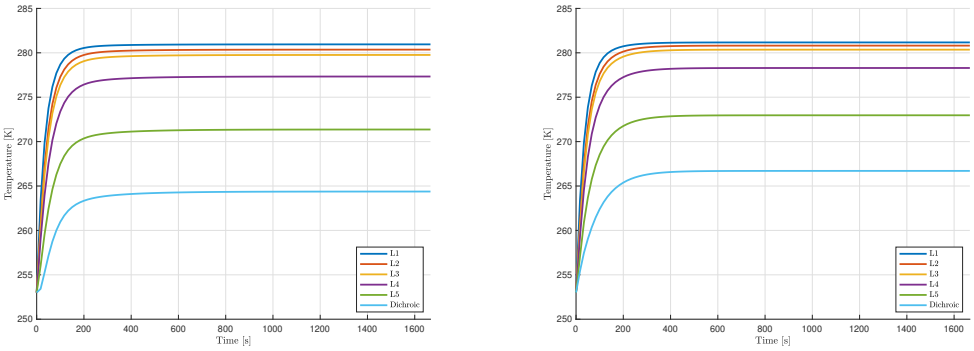

(a) *Case 6* (b) *Case 7*

Figure 5.21: Lens temperatures

5.4. Future steps

These analyses served as a review of the phase-A design of the LUMIO-Cam. The conclusion are that the design allowed the instrument to satisfy some of the requirements (survivability of detectors to direct Sun exposure and overall payload survivability in non-operative conditions) but it also requires further fundamental in depth study to solve residual inadequacies (highlighted in the preliminary operative analysis).
The next steps towards a fully compliant design are: updating the model to include the changes coming from the SRR and performing extensive analyses. These in-depth analyses will ensure that all components satisfy the requirements under every circumstance.
The elements requiring particular attention are:

- The detectors, the thermal links between the focal planes and their support and between the support itself and the other components shall be designed to minimize the heat transfer to the sensitive elements. This would facilitate the task of the thermo-electric coolers.
- The TECs, a proper tuning of the control logic must be defined to maximize their efficiency reducing the electric power needed and the waste heat produced.
- The optical barrel, since the temperature difference between the FPAs and the first lens in the preliminary operative analysis results high, the design shall be modified to improve the passive cooling of the lenses.
- The radiator, the design of this element is the trade off between the needs of the payload designers and the limits of the platform provider.
- Other electronic components (boards), up to now given the preliminary nature of

the analyses, these components were given marginal importance. It is however fundamental to keep every electronic component in the adequate temperature range to ensure optimal performances.

In conclusion, the final output of phase-B should be a complete design of the instrument that allows it to satisfy all requirements. Building this kind of model would allow to perform multi-physics analyses in phase-C considering thermal, mechanical and optical aspects all together.

Bibliography

[1] G. Merisio, F. Topputo, Icarus, https://doi.org/10.1016/j.icarus.2022.115180

[2] F. Topputo, Icarus, https://doi.org/10.1016/j.icarus.2022.115213

[3] G. Merisio, C. Giordano, V. Franzese, F. Topputo (3 March 2021) *LUMIO Phase A, Mission Requirement Document*, Politecnico di Milano, Italy, 1.7

[4] C. Giordano, V. Franzese, G. Merisio, F. Topputo (29 January 2021) *LUMIO Phase A, Mission Analysis Report*, Politecnico di Milano, Italy, 1.6

[5] A. Menicucci, K. Woroniak, E. Bertels (3 March 2021) *LUMIO Phase A, Environmental Design Specification*, Politecnico di Milano, Italy, 1.3

[6] G. Merisio, C. Giordano, V. Franzese, K. Woroniak, E. Bertels, A. Cervone, S. Speretta (12 February 2021) *LUMIO Phase A, System Requirements Document*, Politecnico di Milano, Italy, 1.3

[7] B. Bosman, A. Paskeviciute, K. Woroniak, E. Bertels, A. Cervone, S. Speretta, A. Menicucci, D. Labate, G. Pilato, A. Kukharenka, A. Thorvaldsen, G. Merisio, C. Giordano, V. Franzese, M. Massari, F. Topputo (8 March 2021) *LUMIO Phase A, System Design Report*, Politecnico di Milano, Italy, 1.2

[8] C. Giordano, G. Merisio, (12 February 2021) *LUMIO Phase A, Final Report*, Politecnico di Milano, Italy, 1.0

[9] Leonardo electronics, (25 January 2021) *Technical Note on LUMIO's Optical Desig, LUMIO-LDO-TN-001*, Leonardo S.P.A., Italy, 2.0

[10] James K. Harrison, Daniel W. Gates, James R. Watkins, Billy P. Jones, (26 August 1966) *Lunar Thermal Environment*, NASA George C. Marshall Space Flight Center Huntsville, Alabama

[11] David G. Gilmore Editor, (2002) *Spacecraft Thermal Control Handbook, Volume I: Fundamental Technologies*, https://doi.org/10.2514/4.989117

[12] https://www.nasa.gov/planetarydefense/neoo

[13] https://neliota.astro.noa.gr

[14] V. Franzese, A. Rizza, F. Piccolo, P. Panicucci, G. Merisio, A. Cervone, F. Topputo, L. Provinciali, D. Paglialunga, G. Pilato, M. Pancalli, D. Labate, A. Negri, G. Cucinella, A. Locarini, L. Gomez-Casajus, A. Morselli A. Thorvaldsen, J. Heywood, (3 March 2023) *LUMIO Phase B, System Requirements Document*, Politecnico di Milano, Italy, 2.1

[15] Teledyne Technologies, *CCD201-20 Datasheet*

[16] Incropera, DeWitt, Bergman, Lavine, *Fundamentals of Heat and Mass Transfer*, JOHN WILEY & SONS, U.S.A., 6.0

[17] Leonardo electronics, (17 March 2023) *Technical Note on LUMIO-Cam: LUMIO-Cam ICD, LUMIO_B-LDO-TN-001*, Leonardo S.P.A., Italy, 4.0

List of Figures

List of Tables

Acronyms

Acronym	Description
ADCS	Attitude Dynamics Control System
AU	Astronomical Unit
BOL	Begin Of Life
CCD	Charge Coupled Device
CME	Coronal Mass Ejection
DTE	Direct To Earth
EOL	End Of Life
EPS	Electric Power Subsystem
FD	Finite Difference
FDIR	Failure Detection Identification and Recovery
FoV	Field of View
FPA	Focal Plane Assembly
GMM	Geometrical Mathematical Model
HDR	Hold Down and Release
HIM	Halo Injection Maneuver
ISL	Inter-Satellite Link
L2	Second Lagrangian Equilibrium Point
LUCE	Lunar Cubesat for Exploration
LUMIO	Lunar Meteoroid Impact Observer
Nav&Eng	Navigation and Engineering
NEO	Near Earth Object
NIR	Near Infrared Waveband
OBPDP	On Board Payload Data Processing
PL	Payload
RCS	Reaction Control System
RW	Reaction Wheel

Acronym	Description
SADA	Solar Array Drive Assembly
SEE	Single Event Effect
SMIM	Stable Manifold Injection Maneuver
SNR	Signal to Noise Ratio
SRD	System Requirements Document
SRR	System Requirements Review
TCS	Thermal Control System
TD	Thermal Desktop
TEC	Thermo-Electric Cooler
TID	Total Ionizing Dose
UHF	Ultra High Frequency
VIS	Visible Waveband